PEOPLE
MARIE CURIE ACTIONS
International Outgoing Fellowships (IOF)
Call: FP7-PEOPLE-2011-IOF

Periodic Report

Periodic Report:	Issued in July 2016
Period of Reference:	01/03/2015 – 29/02/2016

"FAEFID"
"Fuel Additives Effect on Fuel Injector Design"

Project Acronym:	FAEFID
Grant Agreement Number:	300410
Beneficiaries:	City University London, UK
Coordinator:	Prof. Manolis Gavaises, City University London, School of Engineering and Mathematical Sciences (SEMS), Northampton Square, EC1V 0HB London, UK
Authors:	Nicholas Mitroglou, City University London (SEMS)
Commencement Date:	01/03/2013
Completion Date:	29/02/2016

Contents

1 Abstract

The primary objective of this research fellowship is the characterisation of the effect of Diesel fuel additives on internal nozzle flow and the emerging spray. Understanding of such behaviour will enhance the design of Diesel injector nozzles, as well as, the development of fuel additives, resulting in improved designs that take advantage of the newly developed additives towards a clean internal combustion engine and environmentally friendly operation.

During the initial stage of this research, a wide search in the related available literature was conducted, so that the fellow could familiarize himself with the state of the art additive technology, its effects (if any) on injector operation and with measurement techniques of fuel physical properties. This literature review showed that not only the available material concerning fuel additives were very few, but also chemical composition of additives was not public (as proprietary) and Diesel fuel measurement techniques (with required accuracy) dictated manufacturing of devices that proved expensive and could not be funded. Following this period, a number of decisions were made. Primarily, the most appealing Diesel fuel additive packages were chosen for future work, based on knowledge acquired through the literature review. Secondly, it was decided to ask for a partner's support on additised fuels supply and characterisation; the fellow has been successful in securing this support and as much of insight as possible on additives technology. Furthermore, the fellow looked for possible collaborators in measuring fuel physical properties in extreme fuel pressure conditions.

In the second stage of the research activity, the fellow started the experimental activity, as well as, the design (where applicable) of future activities. The fellow has managed to successfully measure physical properties of the chosen Diesel fuels at atmospheric pressures and ambient temperatures. Moreover, experiments continued according to the initially proposed plan, however, results were not promising, and proved highly inconclusive. However, all indications pointed towards a strong interaction between additives and cavitation initiation and development. Therefore, a strategic decision was taken to shift the focus of this programme towards fundamental study of cavitation of additised fuels. The latter included the design of a prototype nozzle and the replacement of a task in WP4 with an exotic measurement technique, that of providing density measurements utilising x-rays and computed tomography. At this point it should be highlighted that these actions were not initially described in the proposed WorkProgramme, but the CITY group in collaboration with the scientist in charge from the outgoing host (SBU) believe that these changes are of added value as they have not been conducted before focusing on such application.

During the final year of this programme, the fellow has followed the modified work plan and completed all the associated tasks. Following the successful design of the experimental device certified by the preliminary experiments, the fellow completed high-speed visualisation of internal fuel flow and conducted successfully X-ray computed tomography

(CT) measurements providing liquid volume fraction information inside the flow channel at a resolution of ~15μm. In brief, high-speed imaging identified transient features of the flow that are being studied in detail and provide useful information on string cavitation and vortex shedding mechanisms through bubble detachment and collapse. Additionally, density measurements through micro-CT technique provided quantitative information on cavitation vapour volume fraction (or fuel liquid volume fraction) locally that identify differences among various additives and constitute valuable validation data for computational fluid dynamics (CFD) models development. During this last year of the fellowship, certain CFD models have been developed in order to describe accurately the effect of certain additives on fuel flow.

Finally, during this period, the fellow had the opportunity to disseminate the work undertaken, participating in 6 conferences, while also preparing 5 papers for submission in high respected peer-reviewed scientific journals. The collaboration between the fellow and researchers from highly respected Universities and national US laboratories for facilitating a micro-CT experiment on Diesel fuel flows was also a highlight of this period, mainly due to the joint work which was needed for design and safety needs.

2 Results per WP

WP1 - Objectives: Literature review.

D1: Interim report on literature findings.

The growth in Diesel additive use reflects largely the impact of growing Diesel fuel demand and the changing technology of Diesel engines. In the early days of Diesel engine development, cold starting and ignition quality were major development issues. One of the earliest Diesel fuel additives employed was an ignition improver, still in use today, which greatly assisted in overcoming these problems. Also, the introduction of wax crystal modifiers, or cold flow improvers, was critical to increasing Diesel fuel availability globally. Following the success of additives in the early years of Diesel engine development, additives remained the first and only measure to fulfill either technological improvements that required a high quality Diesel oil, or abide to legislations that were brought from the regulating bodies. In brief, the need to use a greater portion of the crude barrel to produce increased volumes of middle distillates resulted in lowering Diesel's quality; the anti-measure was the introduction of a cetane improver additive that helped in overcoming the above burden and deliver fuel of the required ignition quality. Additionally, recent environmental legislation has reinforced the need for deposit control additives to keep the engine clean and maintain long-term vehicle emissions performance. Moreover, the introduction of very low Sulphur fuels led to the need of lubricity additives, conductivity improver additives and others to improve oxidation stability. Additives can be sub-divided in terms of their point of application as follows [1]:

- Refinery products
    - Antioxidant and stability improver additives

    - Cetane enhancing additives
    - Cold flow improver additives
    - Metal deactivator additives
    - Dyes
- Distribution system products
    - Corrosion inhibitors
    - Pipeline drag reducing additives
    - Anti-static additives
- Automotive performance enhancement products
    - Deposit control additives
    - Cetane improvers
    - Lubricity additives
    - Friction modifiers
    - Antifoam additives
    - Corrosion inhibitors
    - Demulsifiers
    - Fuel borne catalysts for particulate filters

Almost all diesel fuel sold commercially contains additives that are necessary to maintain efficient FIE operation, engine performance and reduce emissions. Due to their proprietary nature and relatively complex chemical structures, additives and mechanisms by which they affect injector flow and/or spray formation are not yet well-known. Detergents are one of the most important components in a diesel additive package and are used for deposit control purposes [2]. Their mechanisms include keeping new injectors clean by generating a protective film on metal surfaces and by preventing agglomeration of deposit precursors, as well as cleaning up fouled injectors by deposit removal and dispersion [3]. Chemistries used for deposit control applications are not unlike household detergents in their basic structure, comprising of an oleophilic tail for good solubility in Diesel fuel, and a polar head to attach to surfaces such as metal and deposits. Detergents can be classified by their structure of the polar head as amines, imidazolines, amides, fatty acid succinimides, polyalkylene succinimides, polyalkyne amines and polyether amines. Surfactants patented for use in direct injection Diesel applications include Polyisobutylene Succinimides (PIBSI). Alkyl quaternary ammonium salts have also been disclosed based on Polyisobutylene (PIB) as well as polymeric quaternary ammonium salts. Recently, a significant and unexpected increase in power was reported with the use of fuel containing specific quaternary ammonium salts [4-6]. PIB-based quaternary ammonium salts at a treat rate as low as 500 ppm and 1000 ppm resulted in a significant power gain compared to unadditised fuel. The mechanism by which the increase in power was achieved is not known. The effect of these additives on injector flow has not been investigated. Understanding the mechanism by which these additives can improve engine power output could be crucial to the development of improved injector designs, injection strategies and additives.

Based on the facts detailed in the previous paragraph, it was decided to examine three different types of Diesel fuel, a Base Diesel that contains no additives, an additised Diesel fuel containing the traditional deposit control additives and, finally, an additised fuel that is

enriched with PIB-based quaternary ammonium salts that have shown unexpected behavior.

WP2 - Objectives: Design/adaptation of suitable properties measurement techniques.

D2: Interim technical report on measurement devices and measurement of properties of additised Diesel

Deposit control additives concentration in Diesel fuel does not exceed ~500ppm, according to Diesel fuel technology reviews [1]. Thus, a dramatic change in physical properties is not expected; however, given the nature of detergents and their designated mode of action, physical properties of additised fuels should be known in both, ambient and elevated pressure conditions, that is also their operating environment.

The fundamental challenge then becomes the reliable measurement of additised fuel properties including density, viscosity, surface tension, thermal conductivity, and heat capacity at injection pressures (P) in excess of 2000 bar and elevated temperatures (T) [7]. Existing density and viscosity databases are predominantly limited to less than 1000 bar and 200°C. The most common high-P, high-T density measurement techniques are the vibrating-body, which is also used for viscosity measurements, the bellows, and the floating piston methods. Although uncertainties can increase above 1.5% at temperatures above ~125°C with vibrating body methods [8, 9], this approach has been used successfully to generate accurate density and viscosity data for select paraffins, aromatics, and naphthalenes. In addition, the vibrating body technique is an experimentally sensitive and non-trivial method to commission. The bellows technique, strictly for density determination, measures the change of fluid volume and is capable of operation at ultra-high pressures at modest temperatures [10, 11]. However, the bellows can fail with repeated use and extended exposure to high temperatures, and it is not possible to observe liquid-solid phase changes that may occur when pressurising the fluid. Hence, a floating-piston densitometer is rendered appropriate for density experiments since this technique is robust at extreme P-T conditions [12] and phase behaviour measurements can be performed with the same apparatus, which is especially important when light gas-heavy hydrocarbon mixtures are investigated. Likewise, a rolling ball viscometer is most suitable for measuring fluid viscosity at extreme P-T conditions since this viscometer is similar in design to the densitometer, it operates to 3000 bar and 260°C, and it allows for visual determination of the fluid of interest. This method has been used [13] to extend the P-T range of data for long-chain, normal alkanes and a branched phthalate. Interfacial tension (IFT) measurements are also crucial and should be performed at extreme P-T conditions. There is a modest amount of high pressure IFT data available in the literature, typically with N_2 plus a paraffin or with water [14], although these data rarely exceed 500 bar and elevated temperatures.

Data on fuel thermal properties at high P-T conditions can be obtained using a transient

plane source (TPS) technique [15], where the "metal strip/strain gauge", which serves as the heat source and temperature sensor, can be suspended or mounted directly in a high-pressure, windowed cell. The thermal conductivity, thermal diffusivity, and specific heat of the fluid is obtained from TPS measurements, although care must be exercised to avoid expanded uncertainty in the thermal properties, as described by Warzoha and Fleischer [16]. Not surprisingly, data on fluid thermal properties is scarce, especially at the extreme P-T conditions of interest.

The relevant literature survey has dictated that measurement of physical properties at elevated pressure and temperature is not a trivial task. Moreover, the devices that ensure minimum error measurements are complex and require extensive financial support that is not available in the current project. Therefore, a decision was taken to perform measurement of physical properties at ambient (atmospheric) pressure and temperature at our premises and exploit our network of collaborators in order to identify laboratories that have these measurement capabilities.

The analysis conducted showed that the Base Diesel fuel and the additised Diesel fuel that demonstrated the power gain effect [4], share very similar, almost identical properties. In detail, all measured properties can be found in the following Table 1.

Table 1: Measured physical properties at ambient conditions

	Base Diesel	**Additised (power gain) Diesel**
Density (kg/m³) @ 15°C	833	832.9
Viscosity (cSt) @ 40°C	3.2491	3.1504
Surface Tension (mN/m) @20°C	28.9	27.6

As illustrated in Table 1 above, the two fuels share almost identical density at ambient conditions. Furthermore, the difference in viscosity between the Base Diesel fuel and the additised fuel with different behaviour is only 3%. Finally, a small disagreement is found in surface tension. The latter was measured in the lab utilising a capillary tube and a high resolution digital camera; post processing of the acquired data showed that the additised fuel with the different flow behaviour, compared to the Base fuel, has a lower surface tension of approximately 4.5%.

WP3 - Objectives: Quantify the effects of additives on fuel injector performance.

D3: Interim progress report on the effect of several physical properties of Diesel blends on needle valve lift, flow rate, operating temperature and injection pressure variations

Initially, assessment of the change in flow rate through the injector was attempted for the Base Diesel and the additised Diesel that showed increased flow rates and engine power

gain. It was decided to use an injector that is almost identical to production fuel injection equipment in a high-pressure common rail system that is identical to the ones in production. This decision was taken in order to fulfil two requirements: (a) to operate the injector as it would have operated in an engine environment, with transient needle valve response, but with the ability to specifically control injection duration, and (b) to inject at as high pressure as modern systems. Thus, the system was built to achieve a maximum injection pressure of 2000 bar and its control software (written exclusively by the fellow) was able of altering the injection duration from a minimum possible duration of 0.5 ms to a maximum of 10ms, simulating almost steady state flow through the nozzle. Moreover, the system had the provision of driving the injector at single, double and in general, multiple injection events in order to assess the effect of the extremely transient behaviour on to the flow rate measurements.

The selected injector was a multi-hole injector nozzle; a design almost identical to the ones found in the market. The general geometry of the injector nozzle is illustrated in Figure 1. Furthermore, a second nozzle geometry was utilised, featuring only a change in the injection hole design; the first nozzle is equipped with cylindrical injection holes of 0.160 mm diameter, while the second design features a tapered injection hole shape where inlet hole diameter is 0.160 mm and outlet diameter is 0.140 mm, resulting in a tapering k-factor of 2. Additionally, the nozzle had a radius of curvature at the inlet of the injection hole that was approximately 0.025 mm. Finally, the needle valve full lift value was 0.300 mm.

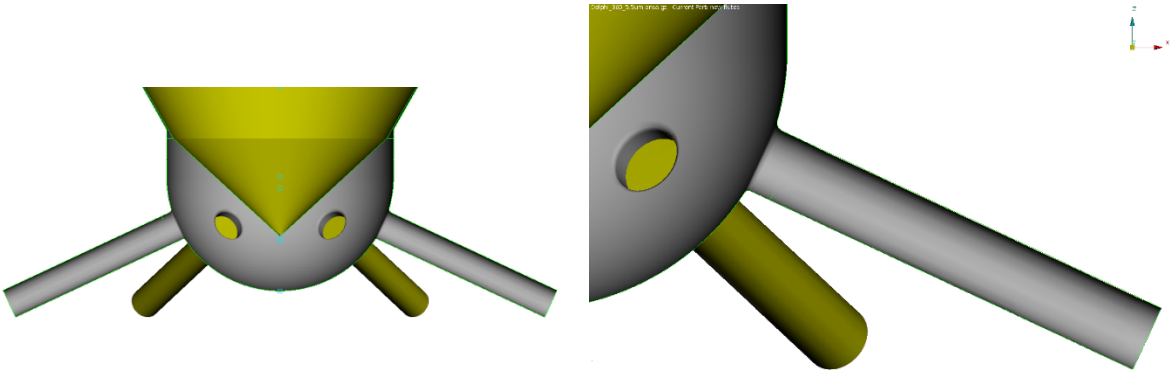

Figure 1: Cut out of the injector nozzle geometry used.

The measurement procedure was designed to provide the average fuel mass injected per stroke. An accurate measurement was ensured by a dedicated mass fuel flow rate device that featured a sensitive balance and monitored continuously the change in fuel mass in a small reservoir. The amount injected per stroke is relatively small and the error in measurement could have been significant, thus, we decided to acquire and monitor the fuel mass after and during 1000 injection events and, consequently, average the values recorded. The test cases selected for both fuels and both nozzle designs are summarised in Table 2; it is worth mentioning that similar test was conducted with the third fuel of choice, an additised (Deposit Control Additive – DCA) Diesel fuel that showed no change in measured flow rate due to the fact that its chemical composition was based on the

traditional DCA components.

Table 2: Test cases

	Cylindrical nozzle	**Tapered nozzle (*k* = 2)**
Base Diesel – Fuel_1	P_{inj} = 800 (850) – 1800 bar t_{inj} = 0.5 – 1.5 ms	
Additised Fuel – Fuel_2 (with recorded effect on flow rate)		

Prior to presentation of the results, it should be mentioned that the initially selected shortest injection duration timings of 0.5 and 0.7 ms were only applied in conjunction with the 800 bar injection pressure to the cylindrical nozzle. The reason lies in the inconsistent results obtained for the minimum injection durations of 0.5 and 0.7 ms. Judging from the results with the above combination on the operating conditions, it is evident that the injector fitted with the cylindrical nozzle could not operate adequately in extra low pressure (800bar) and extra short duration (0.5, 0.7 ms). This is attribute to the fact that increased blockage from cavitation that is more pronounced in a cylindrical injection hole, reduced significantly the injected fuel mass, thus, rendering its accurate measurement impossible. Therefore, the minimum injection pressure was increased to 850 bar and the shortest injection duration timings were utilised again for the tapered nozzle, as its inherent cavitation suppression mechanism (due to its shape) caused blockage to be minimum and injected fuel mass to be above a threshold level and its measurement was believed to be adequately accurate.

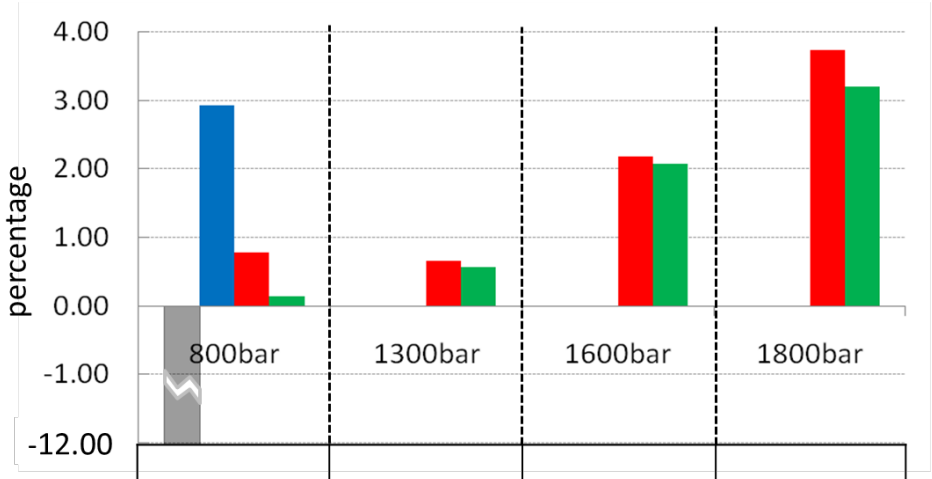

-12.17	-	-	-	0.5ms
2.92	-	-	-	0.7ms
0.78	0.65	2.19	3.73	1.0ms
0.13	0.56	2.07	3.21	1.5ms

Figure 2: Differences in injected fuel mass from the cylindrical nozzle, expressed in percentage in terms of Fuel 2 (additised) - $(m_{Fuel\_2} - m_{Fuel\_1}) / m_{Fuel\_2}$

The above statement can be verified by the summarised results for the cylindrical injection hole nozzle illustrated in Figure 2. It is evident that in the cases of 0.5 and 0.7 ms injection duration the differences in injected mass do not follow a certain trend. Nevertheless, it can be argued that for the remaining injection durations of 1.0 and 1.5 ms, *fuel_2* appears to have a slightly higher fuel flow rate; a difference that increases with increasing injection pressure. The maximum measured difference in injected fuel mass for the cylindrical injection hole nozzle is recorded to be ~3.7% for the additised Diesel fuel, a value that cannot be neglected.

The following injector nozzle to be tested is the one featuring tapered injection holes. The results are summarised in Figure 3. This nozzle design produced results that do not follow the trend set by the cylindrical nozzle. Initially, the shortest injection duration of 0.5 ms appeared to inject consistently more fuel mass of the additised fuel, compared to Base Diesel. The phenomenon seem to be unaffected by the injection pressure and a constant higher measured mass of fuel_2 was recorded that varied from ~2 – 3%. There could be two main factors causing this behaviour; first, the small injected fuel quantities that in the case of 850 bar were of the order of ~10 mg per stroke. However, injection pressures of 1300 bar and above resulted in larger quantities (>20 mg/stroke) for the shortest injection duration; nevertheless, the same trend remains. Therefore, the first conjecture is an extra short duration that effectively means a non-developed and highly transient injection event, affects significantly the injected fuel mass between the two fuels in this tapered nozzle.

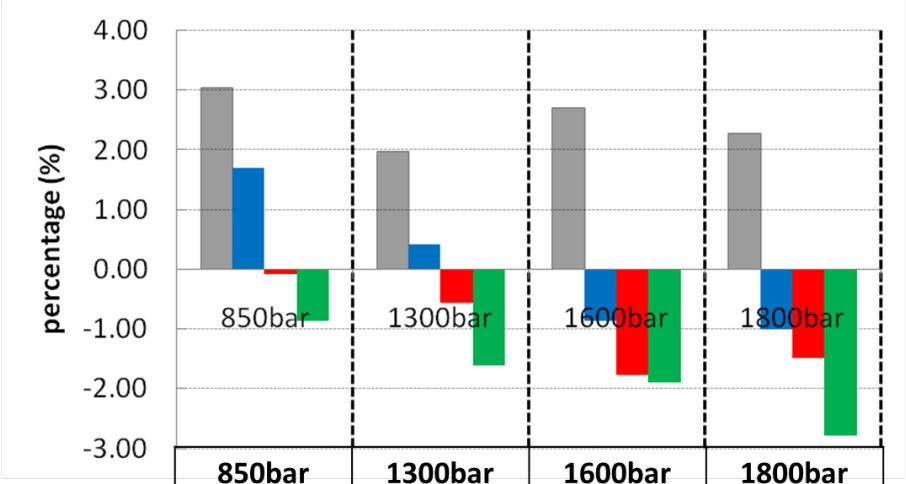

850bar	1300bar	1600bar	1800bar	
3.04	1.98	2.70	2.27	0.5ms
1.70	0.41	-0.86	-1.01	0.7ms
-0.08	-0.57	-1.76	-1.49	1.0ms
-0.86	-1.60	-1.90	-2.79	1.5ms

Figure 3: Differences in injected fuel mass from the tapered nozzle, expressed in percentage in terms of Fuel 2 (additised) - (mFuel_2 – mFuel_1) / mFuel_2

However, this is not the only difference compared to the cylindrical nozzle results presented previously. Figure 3 demonstrates an exactly opposite trend to the one illustrated in Figure 2, regarding injection durations of 1.0 and 1.5 ms and injection pressures of 1300, 1600 and 1800 bar. In this tapered injection hole nozzle, the injected fuel mass measured with the additised fuel is less, compared to the Base Diesel, for as much as 2.8%. Moreover, it is obvious from the graph depicted in Figure 3 that this difference becomes larger as injection pressure increases; furthermore, the same trend is seen in the case of 0.7 ms injection duration, which presents a positive value at low pressures that constantly decreases to even negative values as pressure rises.

Following this observation, one should attempt to explain this behaviour based on the characteristics of the different nozzle design used. It has been mentioned previously that the only change in the two nozzles is the injection hole shape that is cylindrical for the first and tapered for the second nozzle. The effect the tapered injection hole shape has on the flow is described adequately in [17-19] and a summary is illustrated in Figure 4. It is evident from Figure 4 that at low needle valve lifts the pressure gradient at the entrance of the injection hole is more pronounced in the case of the cylindrical nozzle, while it appears to be much limited for the tapered injection hole. Additionally, while at full needle valve lift, the pressure gradient in the tapered injection hole is very smooth and, consequently, it features a cavitation free operation.

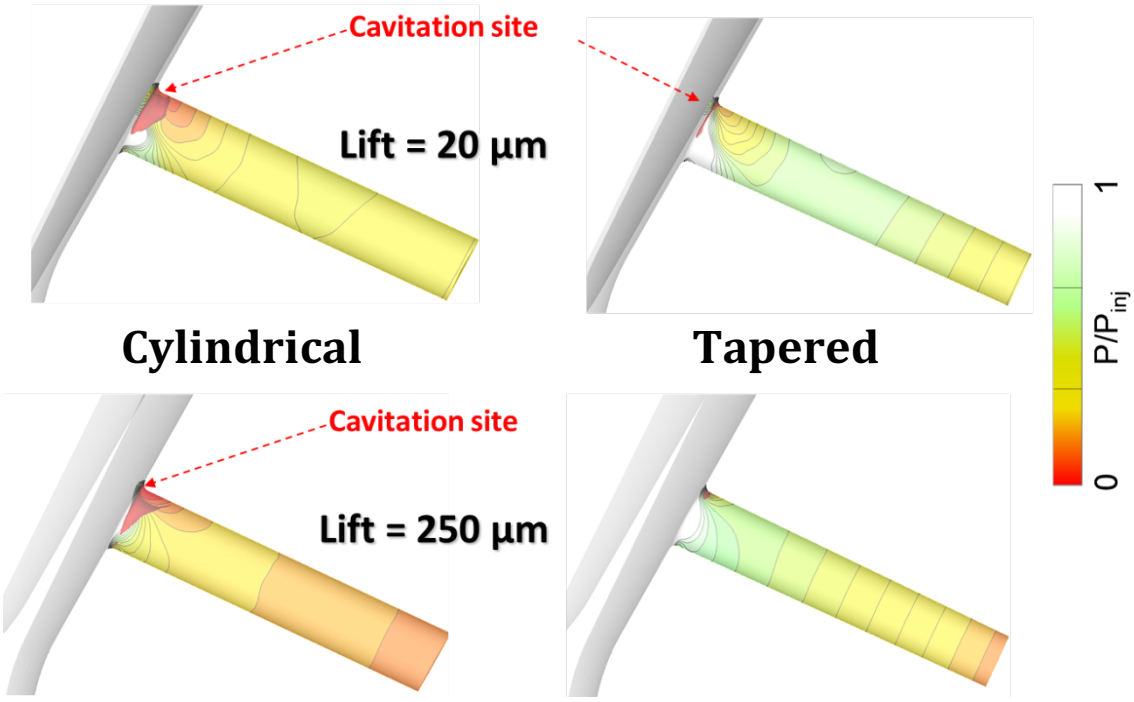

Figure 4: Comparison of the pressure gradient inside a cylindrical and tapered injection holes at two different needle valve lifts; beginning of injection and 20µm lift at top row and full valve lift of 250µm at bottom row.

In an attempt to relate this knowledge to the results acquired in terms of mass flow rate for the two fuels and nozzles, one safely concludes that the small needle valve lift represents a short injection duration event, where the needle valve does not necessarily reaches full lift, instead, it remains at lower lifts for a large percentage of the injection duration. Thus, at injection duration of 0.5 ms even the tapered nozzle will produce a certain amount of cavitation that will decrease as injection duration increases to 0.7 ms and above. In this case, the difference in injected fuel mass is in favour of fuel_2. On the contrary, at long injection durations of 1.0 and 1.5 ms the needle valve stays fully open (lifted) for a considerable amount of time; as illustrated in the simulation results of Figure 4, this is an almost cavitation free region for the tapered injection hole, and, this is found to work in favour of fuel_1. Inevitably, we were led by the facts to relate cavitation initiation and vapour cloud/pocket extend to the changes in the measured mass flow rate for the Base and additised Diesel fuels. Finally, it is significant to mention that increased cavitation pocket sizes inside the injection hole cause the overall flow rate through the hole to drop, as the available effective flow area is reduced by the vapour pocket.

In light of the aforementioned results, and the measured differences in physical properties between the two fuels, we realised there is a change in cavitation initiation and development between the Base and additised Diesel fuels. Therefore, we needed a more fundamental study on cavitation initiation and development in order to capture the different behaviour for both (or more) fuels. Consequently, we designed a custom prototype nozzle that features certain flow characteristics which will enable a fundamental study on

fuel composition/physical properties effect on cavitation. A schematic of the new nozzle design is illustrated in Figure 5, combined with the preliminary simulation results on cavitation volume fraction. In detail, this nozzle features a single injection hole, as we wanted to rule out the complex hole-to-hole flow interactions that are present in a multi-hole nozzle. The dimensions are deliberately chosen to be large-scale for reasons of simplicity and experimental techniques limitations that are explained in the following section. Therefore, the injection hole has a diameter (D) of 3 mm and a length (L) of 10 mm, preserving a normal production nozzle's L/D ratio that is close to 4. Moreover, the injection hole is placed asymmetrically (2.5 mm off-centre) in the upstream gallery, that simulates the sac volume of a multi-hole nozzle. This targets to formation of a non-symmetric flow field inside the injection hole that, in turn, will give rise to cavitation development only on one side of the hole. To strengthen and ensure this result, the needle valve's shape (Figure 5) is also non-symmetric and forces the majority of the fluid to enter the injection hole through one side. Finally, as illustrated in Figure 5, the preliminary simulation results show the formation of a non-symmetric cavitation pocket.

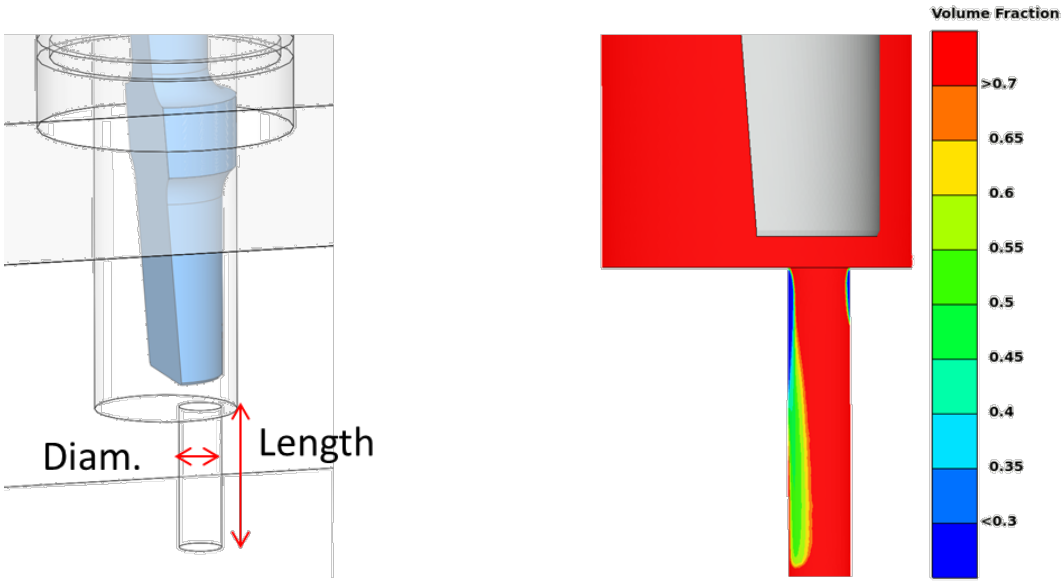

Figure 5: Design characteristics and preliminary simulation volume fraction results for the custom prototype nozzle for cavitation studies.

Initially, this prototype nozzle is intended to be part of a closed-loop flow circuit; thus, utilising injection into liquid and not an open free-spray. Moreover, its operating conditions ($DP = P_{inlet} - P_{outlet}$) are to be kept constant, as is the needle valve that is fixed at various positions, but kept constant throughout an experimental set. The reason of this decision is based on: (i) the highly transient nature of cavitation phenomenon, even at steady-state flow conditions, (ii) the experimental technique limitations that dictate a maximum acquisition rate that is not capable of capturing adequately rapid changes in the flow field and (iii) our desire to isolate and study how the different fuels cavitate at controlled environments.

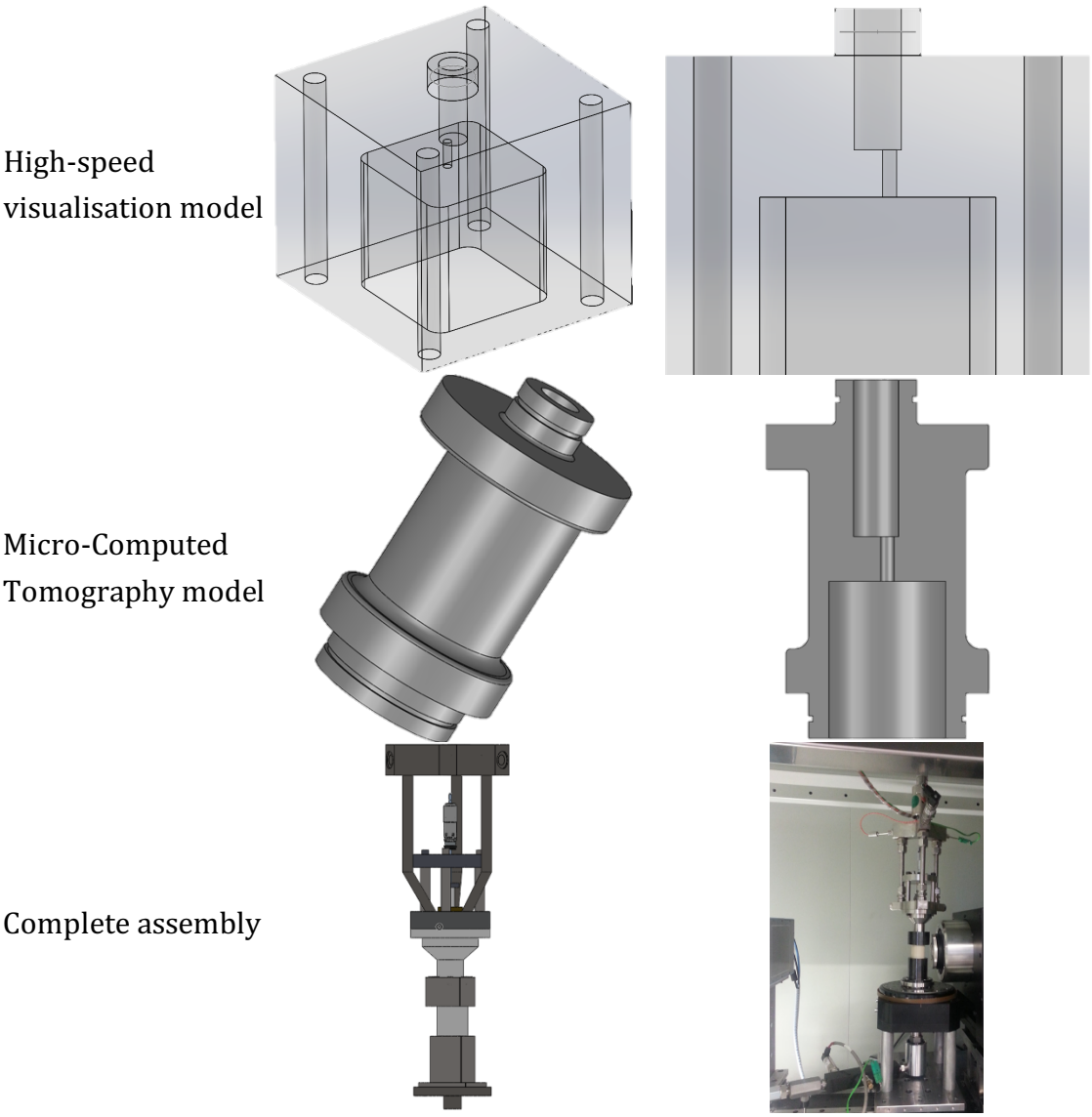

Figure 6: Top row: High-speed visualisation model featuring square outer shape for minimum optical distortion. Middle row: micro CT model featuring injection channel aligned with the axis of symmetry for accurate x-ray measurements. Bottom row: Complete assembly of the system.

The multiple use of this prototype nozzle is illustrated in Figure 6; a square outer design model will be used for ultra-high-speed visualisation studies, ensuring minimum optical distortion through its square outer surfaces, and an axisymmetric model, ensuring identical thickness of material all around the injection channel, will be used for density measurements inside an x-ray computed tomography (CT) device. In detail, high-speed visualisation will provide some insight into the highly transient nature of cavitation development. Our target is to reach frame rates in excess of 50 kHz and be able to capture cavitation pockets development and collapse and their base frequencies. However, plain visualisation only provides qualitatively the extent of a vapour pocket and, additionally, it only captures a projection of the injection channel on to the imaging plane. Therefore, it

would have been difficult, or impossible, to trust these measurements for comparison of subtle differences between Diesel fuels of marginally different cavitation properties. Thus, we decided to exploit the close links of the outgoing host (SBU) to the local Brookhaven National Laboratory (BNL) of the US. The BNL facilities are unique worldwide, as they have just started operating the brightest synchrotron light source, NSLS II. This is an x-ray source of high-power and a variety of x-ray beam outlets, in terms of wavelength, frequency and power, for various research applications. Our ambition is to utilise this equipment and obtain density measurements of liquid and vapour inside our high-pressure injection nozzle prototype. Finally, in conjunction with high-speed visualisation, x-ray density measurements will provide vapour volume fraction measurements and answer the question of "how much" cavitation (vapour) there is inside the injection hole when different fuels are used.

WP4 – Objectives: ~~Experimental investigation on Diesel injector sprays formation and atomisation characteristics and how it is affected by the properties of selected additives~~ Qualitative and quantitative investigation on cavitation formation and development characteristics for various Base and additised Diesel fuels using high-speed shadowgraphy and increased spatial resolution computed tomography (quantitative) technique.

D4: Interim report on the effect of additives on cavitation initiation and extent inside the flow channel.

This work package is the largest and most important of all other packages; it includes the main experimental techniques and produced data that were post-processed in different ways for a variety of extracted results. Therefore, this section will be divided in two main sub-sections, one for high-speed imaging and the second sub-section for X-ray micro-CT.

WP4 – A: High-speed imaging

Two sets of high-speed imaging were performed; the first focusing only on Base Diesel with a camera set-up that provided 50k frames per second and an imaging set-up that was identified as the best choice to image cavitation structures, that provided shadowgraphy images. A sample of the acquired images is illustrated in Figure 7, as a time-sequence of cavitation structures evolution and development. As mentioned above, only Base Diesel fuel was used for this series of experiments at different operating conditions, varying from low to high cavitation numbers (CN), various Reynolds (Re) numbers and different needle valve positions. The acquired data were then post-processed to provide: (i) statistical information on qualitative mean cavitation cloud topology and spatial variability, and (ii) detached bubble clouds frequency of appearance and collapse and their dependence on operating conditions.

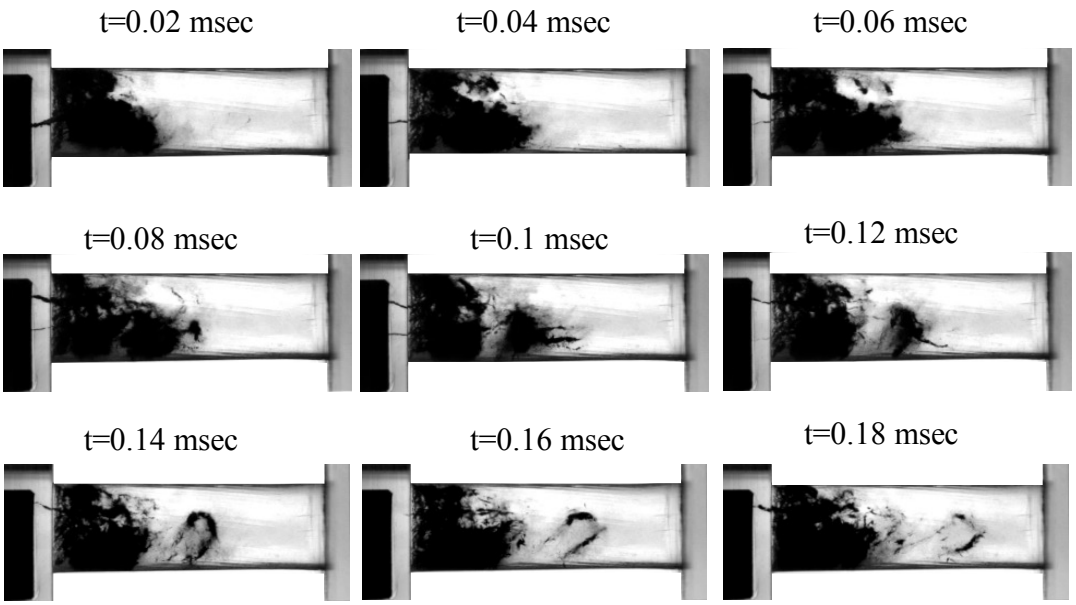

Figure 7: Schematic of the camera view of the injection hole. Time-sequence of cavitation evolution for 0.16 ms for a needle lift of 0.5 mm.

The images presented above represent a sequence of instantaneous single-shot images of the phenomenon. While they do not provide any statistical information on cavitation, they do provide useful insight on several high-frequency phenomena that take place inside this steady-state flow conditions flow channel. These phenomena are: (i) the detachment of bubble clouds from the main cavitation pocket (appears in black), (ii) the collapse of these clouds at locations downstream inside the channel and (iii) string (vortical) cavitation structures that appear to extend from the bottom needle surface (black "obstacle" on the left hand side of the channel entry) until some length inside the flow channel. These transient features of the phenomenon were studied further in an attempt to correlate flow behaviour inside such a confined flow channel to flow over hydrofoils, where this behaviour has been studied [20-22]. Additionally, it is believed that a complementary representation of the results is achieved by averaging 50000 (or 80k) images (of one test case and depending on the frame rate) and present the *mean* cavitation shape and its *standard deviation*. Such processed data images are illustrated in Figure 8, where a collection of three different cavitation numbers (a: CN=1.2, b: CN=1.5 and c: CN=2.1) is illustrated alongside sample instantaneous shadowgraphy images. In the same Figure 8 mean images are illustrated in the middle row, while standard deviation images for the corresponding test cases are seen in the bottom row. The mean cavitation image demonstrates, on a scale from 0 – 1 (intensity), in how many images (out of the 50k/80k) cavitation cloud has been captured at the same location. Effectively, this is translated into the percentage of time (during 1s of set duration) the cavitation cloud is visible and at which location. On the other hand, the standard deviation image displays graphically the variation of the population from the mean location, and it is expressed as variation in image intensity. It is evident from Figure 8 that the transient nature of the phenomenon is captured in the standard deviation

image, as well as, the highly transient cavitation strings that appear at the entrance of the injection channel. Finally, it is clearly seen in the same figure that cavitation cloud is affected dramatically by the CN; as CN increases from 1.2 to 2.1 (from a to c) cavitation cloud extent is increased and the cavitation strings variability is also increased, as seen in the standard deviation contour plots.

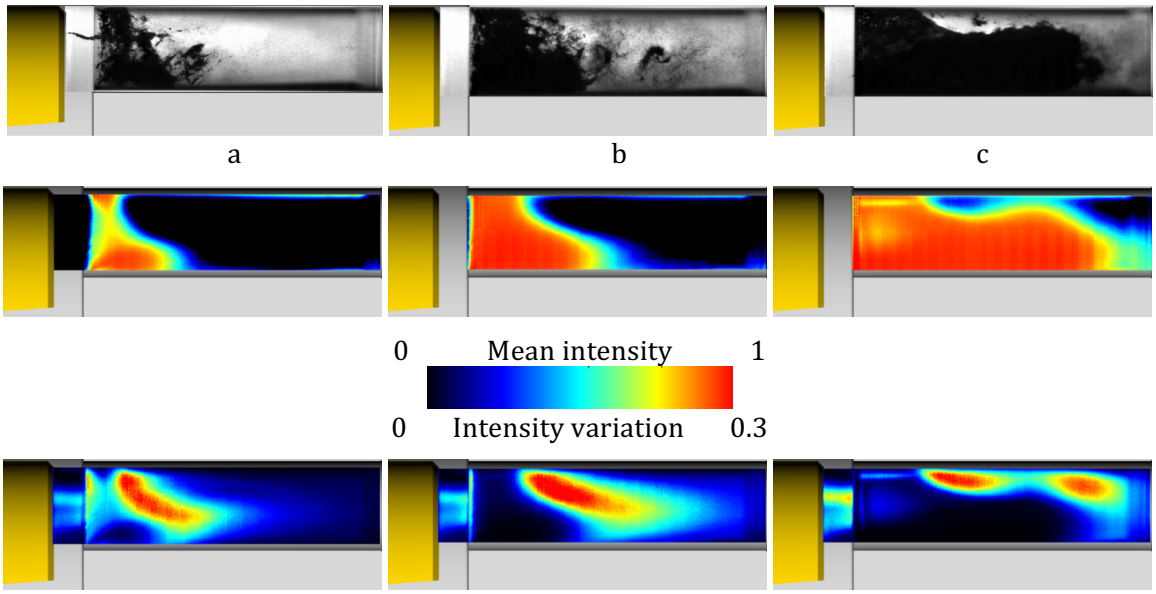

Figure 8: Top row: Instantaneous shadowgraphy images; Middle row: mean intensity images and Bottom row: standard deviation images at at (a) CN=1.2, (b) CN=1.5 and (c) CN=2.1. Mean image colour black (0) means no vapour present, while colour red means vapour present 100% of the time. Standard deviation image represents the deviation from the mean image. Flow time for the above sets is 1s and corresponds to 80k images.

As shown in Figure 9, the needle valve distance to the orifice entrance varies from 2 to 1 mm; the latter has been selected as the nominal lift for the majority of the test cases. The two presented cases share a cavitation number of CN = 1.5 and a Reynolds number that varies between Re = 47k and 55k, for the increased lift and the lower lift case, respectively. Given the expected negligible effect of marginal differences of the Reynolds number on cavitation structures [23], it is evident that presented data are mainly affected by the change in needle valve lift. For both needle lift values, mean images show a very similar cavitation cloud extent; however, standard deviation images demonstrate differences between the two cases. Careful interpretation of the high-speed shadowgraphy standard deviation images at the bottom row of Figure 9 dictates that the higher the needle lift, the more the cavitation cloud instability inside the flow channel. This is clearly shown by the large red-coloured area that presents a variability of ~30% from the mean intensity values. However, the opposite trend is captured for the case of string cavitation visible at the vicinity of the hole entrance; the low needle lift of 1mm shows increased variability compared to the high needle lift of 2mm.

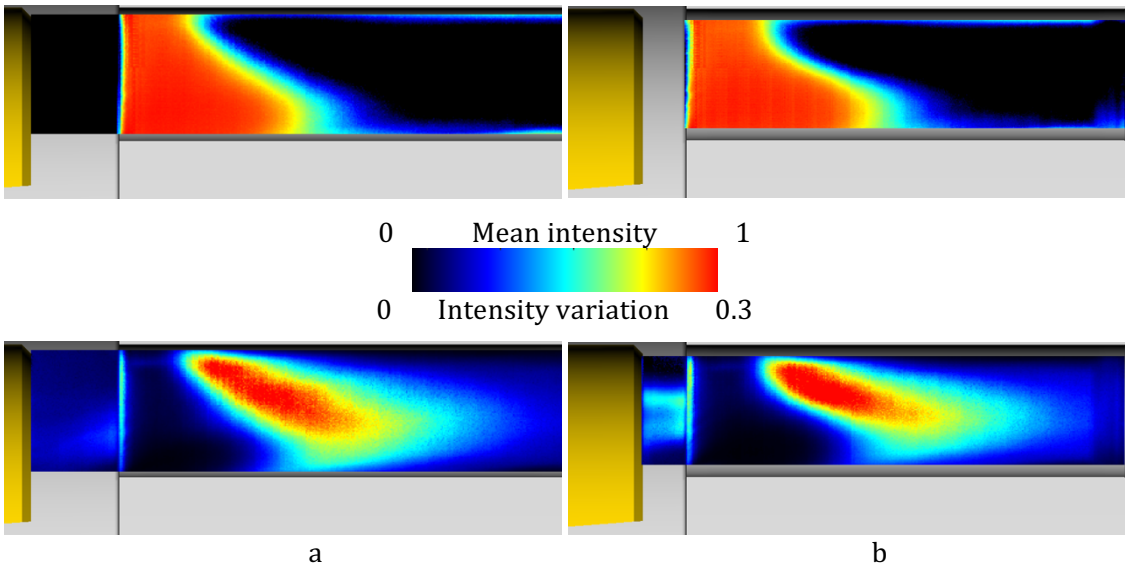

Figure 9: Effect of needle lift position. (a) needle lift 2mm; (b) needle lift 1mm. Top row: mean image; Bottom row: standard deviation image.

Following the qualitative comparison of the effects of CN and needle lift on cavitation structures length and variability, high-speed imaging can provide statistical quantitative information on several transient flow features observed inside the flow channel. Suitable post-processing techniques can quantify: (i) the frequency of detachment of bubble clouds (seen in Figure 7), (ii) the life-time of these clouds inside the channel and (iii) the cavitation string appearance frequency.

Initially, the influence of the cavitation number on the temporal evolution of vortex-cavitation shedding is examined. It is essential to clarify that, based on the current definition of the cavitation number, higher values correspond to a more established cavity pocket downstream of the channel entry. The Strouhal number (=fL/u) was employed as a quantity representative of the shedding frequency f. Initially, the shedding time period was measured as the time interval between the complete detachments of two consecutive vortical clouds. Consequently, the frequency was calculated as the inverse of the aforementioned time period. The nozzle length L and the average flow velocity u in the injector hole, calculated by the imposed flow rate and the nozzle cross-section, were selected as the characteristic length velocity and scales also required for the definition of St. The uncertainty associated with the Strouhal number values was calculated considering the error propagation, due to the uncertainty in the measured values regarding frequency, velocity and nozzle length. The uncertainty in the Strouhal number values in the range 1-5, which is of interest, results in the range 3.3%-4.1%.

Figure 10 illustrates the probability of a vortex-shedding cycle to occur with a characteristic frequency corresponding to a specified value of the Strouhal number. The occurrence probability results as the percentage of the frames where a separation is identified compared to all the frames recorded. Referring to the lowest value of the cavitation number presented in the graph (CN=1.4), a plateau can be discerned in the Strouhal-number

(St=fL/u) values ranging from 2.0 to 3.1, whereas the probability of a cloud separation to occur with each frequency is relatively low and approximately equal to 10%. Hence, the vortex shedding does not justify a clear periodical behaviour, since a dominant shedding frequency (i.e. Strouhal number) does not exist. It must be noted that the Strouhal-number values must be treated as nominal, since they have been defined in terms of an average velocity within the nozzle determined by the imposed flow rate. However, the flow velocity at the contraction region could be significantly higher. On the contrary, the flow obtains a clear periodical behaviour, as the cavitation number increases. The peak probability corresponding to 33% of the recorded cycles can be clearly detected for a value of the Strouhal number approximately equal to 5. Since the probability of cavity cloud detachment in the Strouhal number range 0.1-5.0 is approximately equal to 100%, it can be deduced that the dominant frequency of the phenomenon corresponding to the maximum St is well captured.

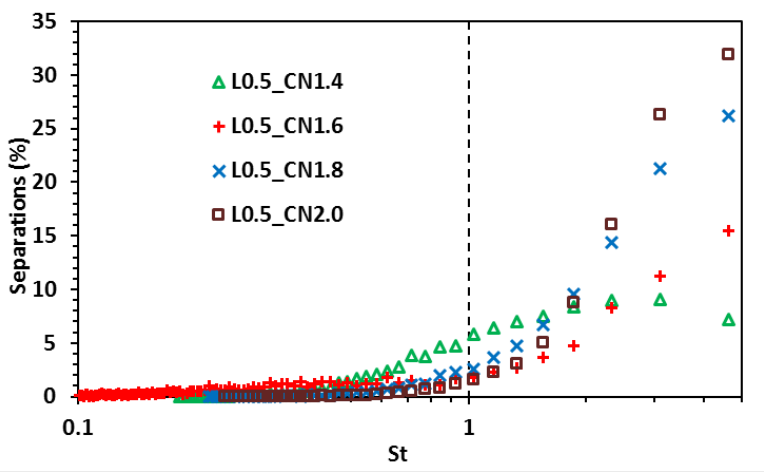

Figure 10: Effect of the cavitation number CN on the temporal evolution of cavitation-vortex shedding for Re=53760 and needle lift equal to 0.5mm

The periodicity of the phenomenon is primarily influenced by the intensity of the re-entrant jet that causes the detachment, which in turn is designated by the cavitation regime (sheet-cloud) and the geometrical layout. The attached cavity is better established for larger cavitation numbers; thus, the adverse pressure gradient in the separated boundary layer becomes steeper and the momentum of the re-entrant jet higher. Since the cloud detachment occurs due to the interaction of the jet with the interface of the attached cavity pocket, the presence of a jet of higher magnitude in the shear layer constitutes the complete separation of a vapour cloud much more plausible. In addition, the presence of more vapour bubbles enhances the boundary-layer vorticity, further enabling the separated cloud to roll up into a coherent vortical structure. It is interesting to notice that the Strouhal-number values characterizing the shedding in the specific nozzle layout are considerably higher than the typical values detected in vortex shedding from hydrofoils, which is in the order of 0.2-0.39. The cause must be attributed to the different cavitation regime, as cloud cavitation prevails, instead of attached sheet cavitation typically occurring in hydrofoils.

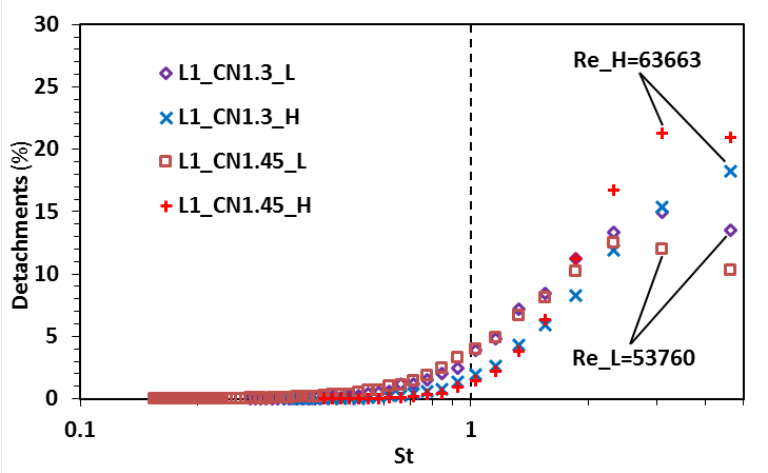

Figure 11: Effect of the main-flow Reynolds number on the temporal evolution of cavitation-vortex shedding for different cavitation-number values and needle lift equal to 1.0 mm

The effect of Reynolds number on the shedding frequency of the cavitating hairpin vortices is illustrated in Figure 11, considering the cavitation number as an additional influencing parameter. Referring to CN=1.3, a single prevailing shedding frequency can be detected, which corresponds to a Strouhal number approximately equal to 3.1 for the lower value of the Reynolds number considered (Re=53760). The vortex-shedding frequency increases with the Reynolds number up to the maximum Strouhal-number value approximately equal to 5.0, while the periodicity of the phenomenon is slightly enhanced since the percentage of vortical structures recorded being shed with the frequency of maximum probability is higher compared to Re=53760 (18% instead of 15%). It must be mentioned that in the test case characterized by CN=1.3 and Re=63663, the shedding probability with a Strouhal number higher than 5.0 is in the order of 27%. Hence, the evolution of the phenomenon could be even more rapid exceeding the temporal resolution of the visualisation technique. The inducement of more rapid vortex shedding is justified, as higher flow velocity leads to a more significant separation downstream of the contraction realised by the needle and needle seat and hence increased levels of vorticity in the boundary-layer region, as well as a steeper adverse pressure gradient producing a re-entrant jet of higher momentum, which reaches the interface of the cavity attached on the nozzle wall in a shorter time period and causes a more frequent detachment of a vapour cloud.

The manifestation of the shedding mechanism in a periodical manner is clearly enhanced with increase of the Reynolds number for a higher cavitation-number value considered equal to 1.45, as also shown in Figure 11. It is interesting to notice that the peak-probability Strouhal number for a specific Reynolds number actually decreases slightly compared to the respective for CN=1.3. In other words, increase of the main flow-velocity seems to favour the cavitating vortices being shed with the lower frequency. This flow behaviour, although counter-intuitive, is in agreement with the observations of [24], which reported that increase of the Reynolds number leads to a shedding sequence of lower frequency due to the agglomeration of vortex cavities that live longer due to the increased cavitation number.

It must also be mentioned that, for CN=1.45, there is a probability approximately equal to 15% the shedding to occur with frequencies higher than the maximum measurable one, which could be indicative of a probability plateau for Strouhal-number values larger than 3.1.

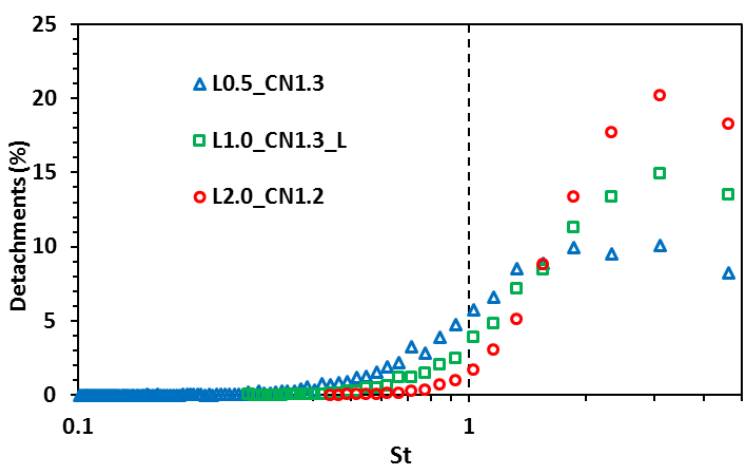

Figure 12: Effect of the needle lift on the temporal evolution of cavitation-vortex shedding for Re=53760

Figure 12 elucidates the influence of the needle lift on the dynamical evolution of vortical cavitation. As it is clearly illustrated, increase of the relative position of the needle in reference to the injection-hole entry from 0.5 to 2.0 mm enhances the periodicity of vortex shedding. The prevailing shedding frequency remains constant and corresponds to a Strouhal value of 3.1 for needle lifts equal to 1.0 and 2.0 mm, respectively, whereas a characteristic frequency cannot be detected for a lift equal to 0.5 mm. This trend can be justified by taking into account that the flow passage becomes narrower as the needle lift decreases (throttling effect). Hence, the flow experiences a more significant blockage prior to entering the nozzle and, subsequently, a more severe expansion within the injection hole. The body of the needle, in essence, acts as an obstacle, which provokes further instability in the already highly turbulent flow. The flow separation downstream of the abrupt geometrical contraction becomes more violent due to the steeper adverse pressure gradient occurring in the contraction region and the sequence of vortex shedding becomes more stochastic. The probability of shedding occurrence with frequencies higher than 25.0kHz, i.e. St≈5.0, is in the order of 3.5%, 11.5% and 9.5% for needle lifts of 0.5, 1.0 and 2.0mm, respectively. It can be therefore justified that the dominant frequency existing for lifts of 1.0 and 2.0mm is well captured by the visualization technique.

It is of high engineering value to be able to accurately pinpoint the locations where detached bubble clouds collapse, as these sites qualify as possible erosion sites. Figure 13 gives insight on the impact of the prevailing flow conditions on the life period and the spatial development of the cavitating vortices that have been found to emerge within the injector nozzle. Initially, the effect of the cavitation number is considered and, as can be seen in Figure 13a, increased values of the specific quantity lead to the onset of hairpin vortices that

travel longer with the main flow and collapse at locations closer to the nozzle outlet. The vast majority of vortices recorded for the lowest value of the cavitation number (CN=0.9) collapse prior to the nozzle mid-length, with a probability peak at a location corresponding to a third of the total length. On the other hand, for CN=1.45 most of the cavitating vortices recorded collapse at a location close to 0.8 of the channel length. This trend is in compliance with the conclusions mentioned in the discussion of Figure 10. A larger cavitation number is indicative of increased intensity of the cavity pocket, as well as increased vorticity in the flow-separation region. Hence, the effect of the cavitation number on the location where vortex cavitation collapses, in essence, also describes the corresponding effect of the vapour cloud length. As CN increases from 0.9 to 1.3, the vortices detaching from the attached cavity trailing edge, which is, in fact, closer to the hole outlet due to the larger extent of the cavity pocket, travel longer with the main flow due to their increased vorticity magnitude and surplus of vapour bubbles and collapse at locations close to the nozzle outlet (L/L0≈0.8). However, it must be noted that increase of the cavitation number from 1.3 to 1.45 does not alter the location, where the peak value of collapses occurs. This must be attributed to the upstream effect of the outlet, which induces flow instabilities that cause the vortex collapse.

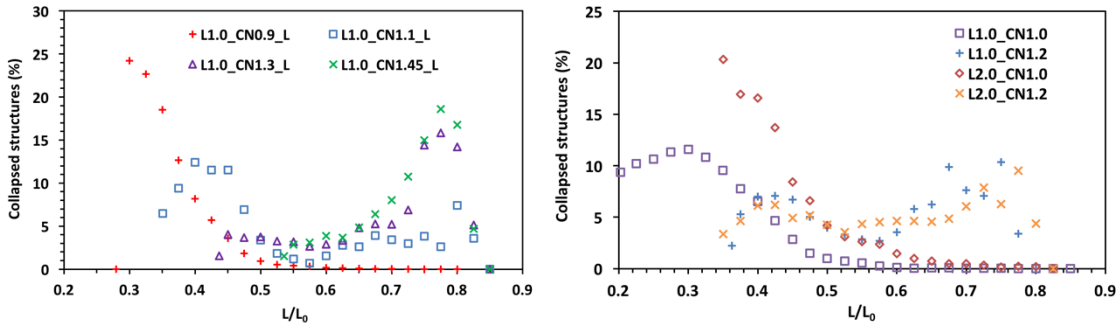

Figure 13: (a) Effect of cavitation number CN on the location of vortex-cavitation collapse for Re=53760 and needle lift equal to 1.0 mm. (b) Effect of needle lift on vortex-cavitation collapse for different values of the cavitation number.

The flow-passage layout is expected to have a considerable impact on the topology of bubble clouds detachment and collapse, since it acts as a controlling parameter for the intensity of both the flow separation downstream of the geometrical contraction and the extent of the cavity pocket developing within the nozzle. The effect of the needle lift on the life period of the cavitating vortices is shown in Figure 13b, where the cavitation number is also considered as a parameter. In reference to the lower cavitation number (CN=1.0), increasing the needle lift from 1.0 to 2.0mm, clearly enhances the magnitude of the vapour vortices, since all the structures recorded collapse at 0.34 of the nozzle length or downstream of that location, whereas in the case of 1.0 mm lift, almost 64% of the recorded vortices have collapsed at locations closer to the hole inlet. Besides, the peak value in the graph (at L/L0=0.34) indicating the location at which the vortex-cavities are most likely to collapse, is more profound in the case of 2.0 mm lift, supporting the conclusion drawn in the discussion referring to Figure 12, that a wider gap between the needle and the needle seat

enhances the periodical nature of the vortex-shedding sequence. It has been made clear that the transient structures emerging inside the injector for low values of the cavitation number and needle lift higher than 1.0 mm, are characterised by a single prevailing onset frequency and have a characteristic life span associated with a high-probability location of vapour collapse.

On the contrary, for CN=1.2, the spatial evolution of the flow phenomena seems to be relatively insensitive to the needle lift, as for increased lift, the pattern of locations, where the detached vapour clouds collapse, exhibits an almost negligible shift toward the nozzle outlet. Besides, the region where vapour collapse has been recorded exhibits a higher scattering compared to the lower cavitation number, spanning along 0.35 to 0.8 of the overall nozzle length. It is also interesting to observe that the most probable location of the hairpin-vortex collapse is detected in the range 0.74-0.78 of the nozzle length, while there is an additional, local maximum value of collapse probability approximately at 0.42. It is postulated that the increased flow instability linked to the higher cavitation number value (CN=1.2) compels the shedding mechanism to be manifested with more than one prevailing frequencies and thus shedding cavities of different magnitude and life span set in, which subsequently collapse at different locations. It can therefore be justified that the cavitation number has a much more considerable impact on the spatial development of vortical cavitation, rather than the geometrical contraction of the flow passage.

Finally, as stated earlier, the collapse locations of these detached bubble clouds are possible erosion sites. The latter statement, as well as the data extracted from the high-speed imaging experiments are fully validated by the X-ray micro-CT data, presented in a following section. In brief, the X-ray tomography extracted flow channel geometry shows wear at specified locations that correspond to the above collapse locations of these bubble clouds.

Apart from the statistical analysis and the effects of operating flow conditions on cavitation, another two factors were examined; these are the effect of dissolved gas in the fuel and the effect of additives on cavitation. It is known that every liquid can dissolve a certain amount of gas content, depending on Henry's constant and temperature. Gas is then found in the form of microbubbles inside the liquid fuel. However, these microbubbles can possible act as nucleation sites for cavitation vapour production or they can be expanded if found in a low pressure region (still above the vapour pressure of the liquid), and create a gas pockets that can be falsely considered as vapour production. In order to qualitatively assess this phenomenon, the fellow de-gassed some of the Base fuel and run several test cases. The de-gassing process followed is summarised in the use of a degassing chamber, a vacuum pump and the empirical vapour pressure-temperature relationships for Diesel fuel given in [25]. As Diesel fuel was stored and degassed at room temperature, its vapour pressure was calculated to be approximately 10k Pa; furthermore, for each de-gassing session, a quantity of approximately 10 litres were brought down to the target vapour pressure and kept under these conditions overnight, i.e., for ~12 hours.

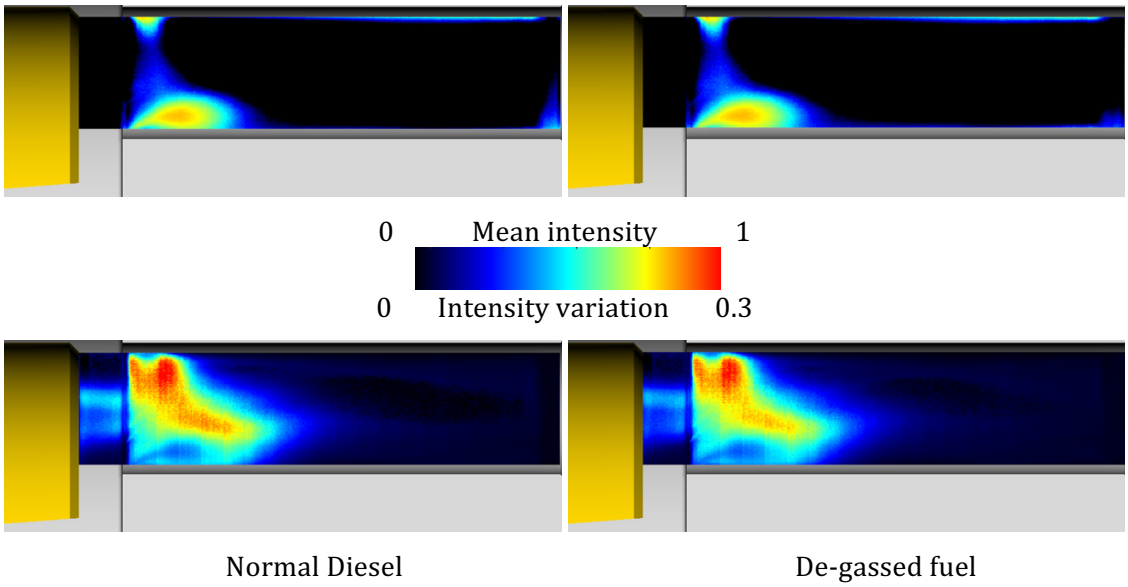

Figure 14: Effect of dissolved gas in fuel at CN = 1.2. Top row: mean image; Bottom row: standard deviation image.

Figure 14 illustrates a direct qualitative comparison between normal and de-gassed fuel for a low CN of 1.2. The selection of a low cavitation number is justified by the fact that we expect to have differences in cavitation pocket size at conditions close to incipient cavitation conditions and not at fully developed and detached vapour pocket. As it is evident from Figure 14, there is no difference in the mean images for both fuels; cavitation topology looks identical. A marginal difference is only visible in the standard deviation images (bottom row), where the variability in vapour pocket size and topology is illustrated. A careful examination of the standard deviation images reveals slightly higher variation in cavitation string structures for the normal Diesel, as well as, marginally larger areas of red(ish) colour, compared to the de-gassed fuel. However, one should only judge on the effect of dissolved gas in the fuel on cavitation structures once the quantitative results of X-ray micro-CT are presented in the following section.

Finally, to conclude the high-speed qualitative visualisation results, the effect of a Diesel additive is presented. This additive is the one responsible for the power gain effect and the increased flow rate reported in the first periodic report and the results of WP3. As illustrated in Figure 15, qualitative results from visualisation studies denote that effectively, there is no visible difference between the two fuels in cavitation vapour pocket topology and variability; both cases of Figure 15 look identical. The same identical behaviour has been recorded for a variety of CN, ranging from 1 to 2, and a variety of Reynolds number settings. Thus, it is evident from the results presented so far that there is well hidden mechanism in the operation of this specific additive that enhances the flow rate without altering vapour creation; i.e. without changing indirectly the channel blockage ratio due to cavitation presence. The answer to the above speculation is probably given in the following section, where quantitative measurements of liquid volume fraction are presented, as part of the X-ray micro-CT study.

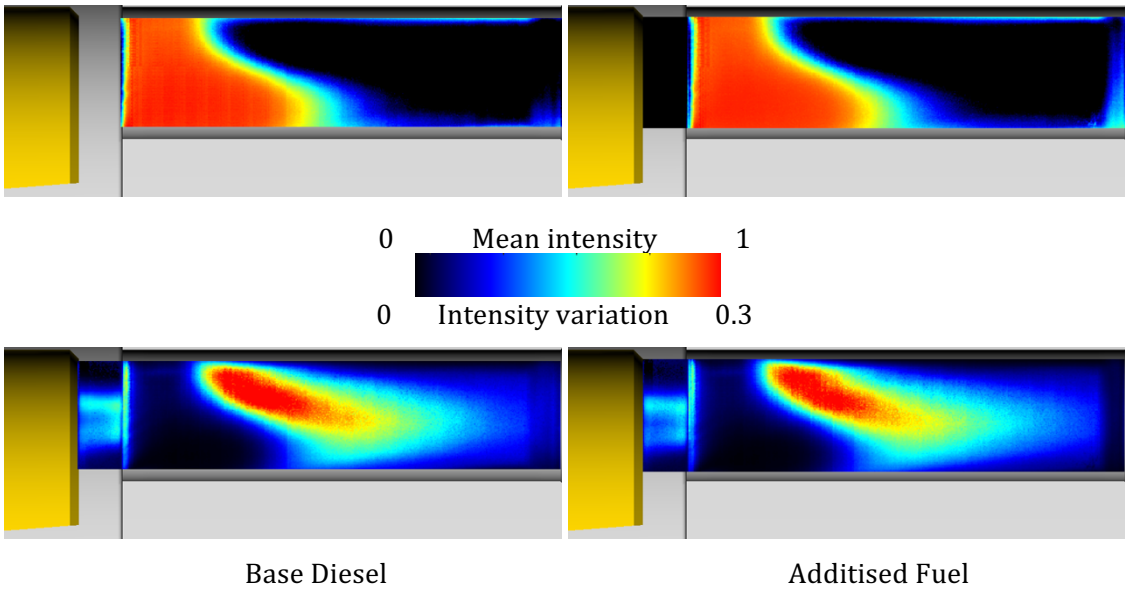

Figure 15: Effect of additive on cavitation structures at CN=1.5. Top row: mean image; Bottom row: standard deviation image

WP4 – B: X-ray micro-CT

The following investigation that has replaced the PDA measurements in WP4, exploits the increased spatial resolution of a cone-beam CT system [26] to quantitatively measure mean, three-dimensional liquid volume fraction inside the custom-design, scaled-up model channel flow that uses Diesel, as the working fluid. Due to the required long sampling times, the obtained ***mean liquid volume fractions*** are compared against ultra-high-speed flow visualisation results to qualitatively assess the dynamic behaviour of the flow. This research programme, and this WP4 in particular, demonstrates the ability of a laboratory scale X-ray source to provide the average, three-dimensional liquid volume fraction and it is able to capture the effects of several flow parameters on cavitation structures present inside the custom injection hole.

As presented below, the observed flow field inside and upstream of the designed orifice has many similarities in cavitation development to that of multi-hole Diesel nozzles. The test-rig has been designed specifically for use inside the micro-CT facility developed at the University of Bergamo (Figure 16c). The needle is set at a fixed position while the pressure difference across the orifice is also constant during one experimental case; tested values ranged from 10 to 40 bar. The hydraulic unit that drives the system is a commercial one, able of delivering a maximum flow rate of 40 l/min. It was modified to accommodate a water–fuel heat exchanger equipped with a temperature control mechanism for accurate Diesel fuel temperature control and monitor throughout the experimental campaign. The fuel temperature did not deviate more than 0.5°C from the set-point that was 40°C, regardless the set pressure level. Initially, the effects of several flow parameters on cavitation inception and development will be presented only with Base Diesel as the working fluid; its properties at 40°C are ρ=850 kg/m3, ν~3.9mm2/s). The effects of Diesel

properties and additives will be presented at the following section.

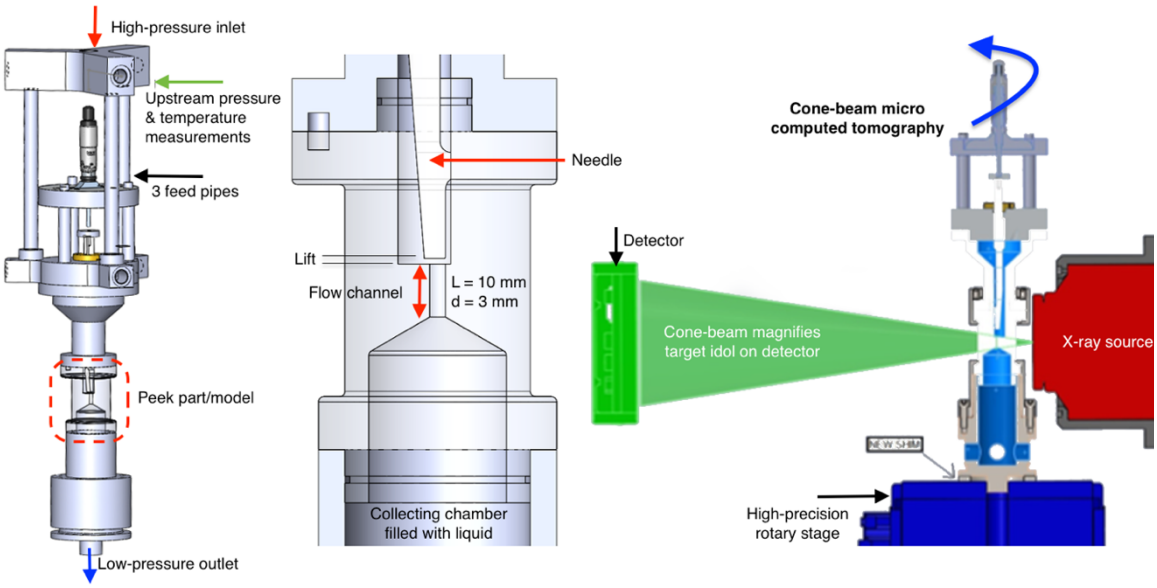

a b c

Figure 16: (a) Overall test-rig set-up; (b) model nozzle cross-section with dimensions, and (c) tomography experimental set-up.

Initially, a direct comparison between flow visualisation and micro-CT results will assist in understanding the flow pattern inside the flow channel and will highlight the certain drawback of any planar visualisation technique, which is the lack of three-dimensional information. Figure 17 is divided in two columns, illustrating high-speed shadowgraphy and quantitative X-ray time-averaged liquid volume fraction measurements at the left and right hand side columns, respectively. Visualisation results at the top-left corner of Figure 17a, have been extensively presented in the previous section of this document; thus, we will focus on X-ray micro-CT results and their comparison to high-speed images. Focusing only on the visualisation sample of Figure 17a, an observer may come to a false-representation of cavitation that seems to entirely block the first half of the flow channel. However, observation of the micro-CT results on Figure 17b, immediately corrects the wrong perception of the flow given previously. The two isometric view representations correspond to the complete channel (one cut at the symmetry plane), as well as, the front view of 80% liquid volume fraction. They demonstrate that cavitation starts as a ring, at the entrance of the nozzle hole, leaving the volume around the axis of the hole available to the liquid flow. As the nozzle model promotes asymmetric flow entry to the orifice, flow velocities and turbulence inside the channel differ from top to bottom. Thus, the cavitation cloud shapes accordingly, as seen at the top micro-CT image of Figure 17b, where half of the channel is illustrated. Low values of liquid volume fraction are observed also at the top of the channel, where cavitation diminishes relatively quickly (almost at the first quarter of the hole length). Similar levels of liquid volume fraction at the bottom of the channel extend further inside the flow orifice up to almost 3/4 of its length.

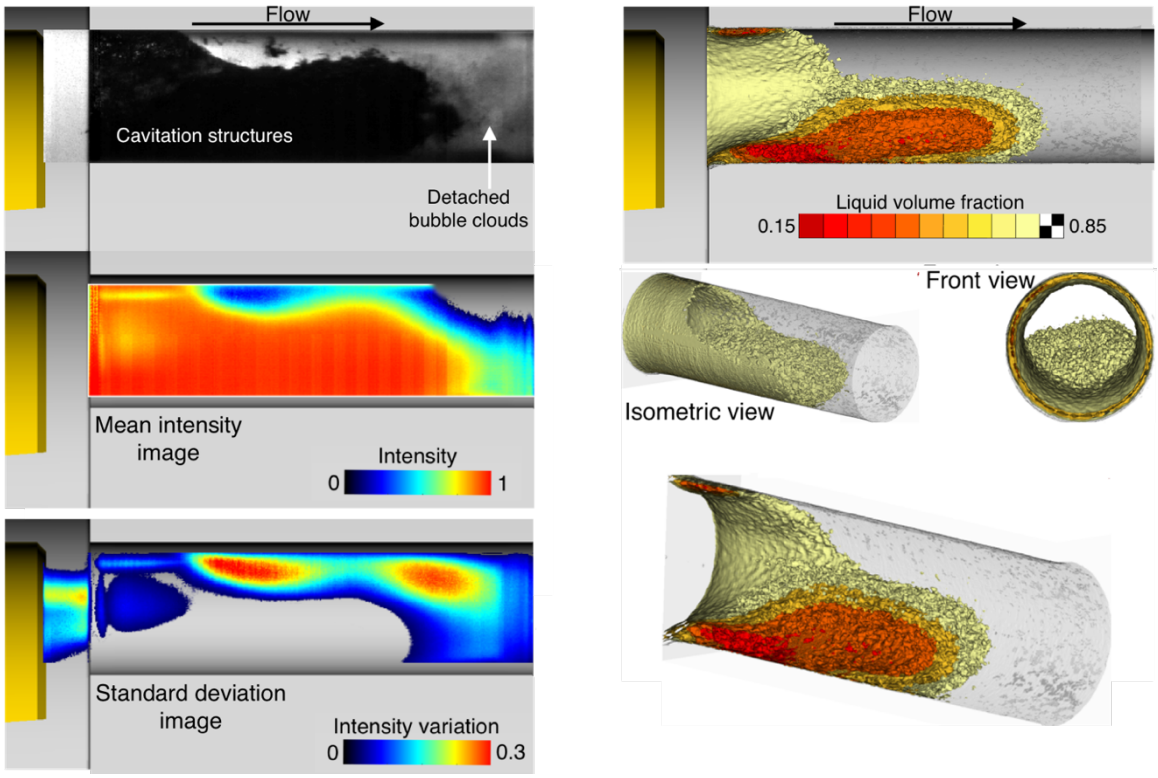

a b

Figure 17: (a) Instantaneous flow shadowgraphy image and corresponding mean and standard deviation images. (b) micro-CT measurements of liquid volume fraction presented as side-view-cut iso-surfaces and isometric and front view images. Flow conditions: CN = 2.1, Re = 55.5k, and needle lift of 1mm].

A direct comparison of shadowgraphy versus micro-CT results is illustrated in Figure 18, where the top row presents an instantaneous, a mean and a standard deviation image of the flow inside the channel at a low cavitation number of 1.5. At the bottom row micro-CT results of the exact flow conditions are presented as contour plot on the symmetry plane, liquid volume fraction iso-surfaces on half-channel and projected vapour volume fraction of the total depth of the channel[1]. In brief, from top left to right, the instantaneous image illustrates a snapshot of all observed flow phenomena inside the flow channel like string cavitation and a detached bubble cloud; the mean image alongside presents a qualitative representation of the vapour cloud and the standard deviation image illustrates the locations with increased variability. On the bottom row, a contour plot of liquid volume fraction on the symmetry plane is displayed on the left, followed by a half channel representation of liquid fraction iso-surfaces and the third image illustrates projected vapour volume fraction. While a plane-cut contour plot quantifies liquid volume fraction as

[1]Exploiting the uniformity of the Cartesian three-dimensional grid, the projected void along the channel length is calculated by a summation of the product of vapour volume fraction at each location (i, j, k) multiplied by the corresponding voxel's volume; the sum is then divided by the square of the cell grid size; it effectively presents a line integral of the non-dimensional quantity (1-αliq) [27-28]

low as 50%, for the presented conditions, cavitation extend does not look similar to an instantaneous flow image. This discrepancy between shadowgraphy qualitative data and micro-CT volume fraction measurements is not minimised even when comparing a half-channel representation with liquid volume fraction iso-surfaces; it is evident from the results that even a liquid volume fraction as high as marginally below 85% is able of blocking the light intensity, in the case of shadowgraphy. However, comparison of the plane-integrated micro-CT results to imaging data proves to be more realistic, as locations with projected vapour fraction marginally larger than 0 μm coincide with that locations of shadowgraphy images that exhibit minimum to zero intensity variability.

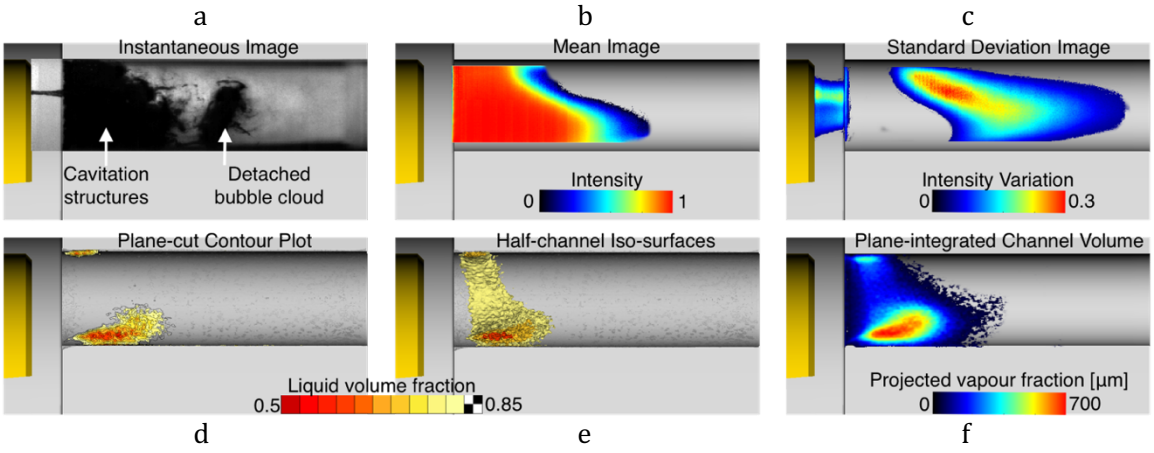

Figure 18: Comparison of high-speed shadowgraphy images versus micro-CT liquid volume fraction. (a) Instantaneous shadowgraphy image; (b) mean cavitation image; (c) standard deviation images; (d) liquid volume fraction on the mid-plane; (e) half-channel liquid fraction iso-surfaces; (f) plane-integrated channel volume vapour fraction contours [CN = 1.5, Re = 55.5k, Cd = 0.7 at 1mm needle lift].

The effect of needle valve lift is examined in figures Figure 19 and Figure 20. In detail, Figure 19 illustrates a direct comparison of micro-CT data (top and middle rows) versus high-speed shadowgraphy (bottom row). As shown in Figure 19, the needle valve distance to the orifice entrance varies from 2 to 1 mm; the latter has been selected as the nominal lift for the majority of the test cases. The two presented cases share a cavitation number of CN = 1.5 and a Reynolds number that varies between Re = 47k and 55k, for the increased lift and the lower lift case, respectively. Given the expected negligible effect of marginal differences of the Reynolds number on cavitation structures [23], it is evident that presented data are mainly affected by the change in needle valve lift. For the 2mm needle lift value, the measurements show a confined vapour distribution, where liquid volume fraction values are as high as 80%. As the needle valve lift is reduced to 1mm (right-hand-side of Figure 19), the developed phenomena become more intense, compared to the high needle lift case. For the case of 1mm lift, liquid volume fraction iso-surfaces denote that cavitation now extends almost up to one third of the hole length and in the core of the created cavitation cloud, vapour volume fraction values are as high as 40%. Finally, interpretation of the high-speed shadowgraphy standard deviation images at the bottom row of Figure 19 dictates that the higher the needle lift, the more the cavitation cloud instability inside the flow

channel. This is clearly shown by the large red-coloured area that presents a variability of ~30% from the mean intensity values. However, the opposite trend is captured for the case of string cavitation visible at the vicinity of the hole entrance; the low needle lift of 1mm shows increased variability compared to the high needle lift of 2mm.

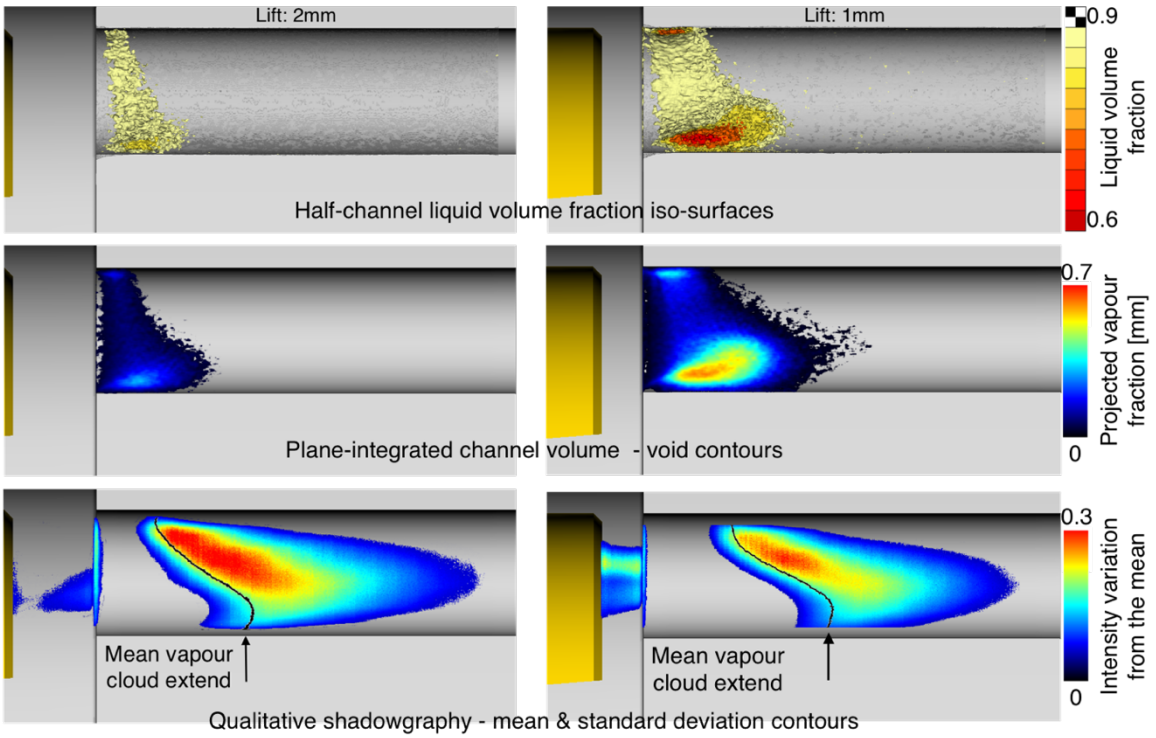

Figure 19: Effect of needle lift position on vapour pockets presented as liquid fraction iso-surfaces for half the channel. Cavitation number is fixed at 1.5 and Reynolds number equals to 47k for needle lift = 2mm and 55.5k for the low needle lift of 1mm.

At even lower needle lifts than 1mm, a similar trend is found and is depicted in Figure 20, where the nominal lift of 1mm is compared against the lowest tested lift of 0.5mm. The flow conditions in both cases are similar sharing the same cavitation number of CN = 2.1 and Re = 55k for the 1mm lift case and Re = 36k for the lowest lift case. This difference in Reynolds numbers is due to the low lift that inevitably limits the flow area available upstream the channel entrance to values lower than the channel's cross-sectional area. Nevertheless, the cavitation number of 2.1 causes extended cavitation in the 1mm lift case, as shown by the contour plot on the channel's symmetry plane; however, as shown in the embedded front view image, there are still locations inside the channel that exhibit either negligible, or no cavitation at all. Despite the lower Reynolds number for the lowest lift case of 0.5mm, the flow picture on the symmetry plane is drastically different to the one of 1mm lift. It is evident from both illustrated views of 0.5mm lift that almost 1/3 of the channel length is occupied by liquid volume fraction ranging from 15% to 60%. Additionally, the area exhibiting extra low liquid volume fraction of ~15% is larger for the lowest lift case, compared to the basic lift of 1mm. Finally, it has been established that needle valve lift has a pronounced effect on cavitation structures, as it promotes turbulence, which, in turn,

promotes cavitation. Unfortunately, the total channel blockage with vapour at the lowest needle lift prevented shadowgraphy data to be collected, as there was no light penetration through the channel due to increased vapour concentration.

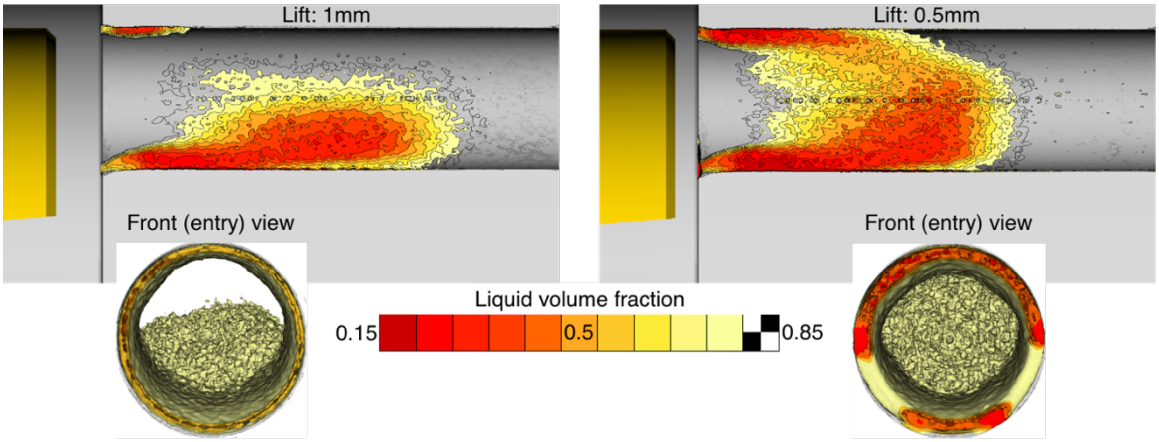

Figure 20: Effect of needle lift position on vapour pockets presented as liquid fraction contours on the channel symmetry plane. Cavitation number is fixed at 2.1 and Reynolds number is 55.5k for the high lift of 1mm and 36.5k for the low lift value of 0.5mm

A direct comparison of the effect of cavitation number on vapour generation is illustrated in Figure 21. At the nominal needle lift of 1mm, left-hand-side of Figure 21 corresponds to CN = 2.1 and it presents, from top to bottom, micro-CT data in the form of half-channel iso-surfaces, plane-integrated channel volume void fraction and high-speed shadowgraphy standard deviation images; the same data representation is illustrated in the right-hand-side of Figure 21 for the lower cavitation number of CN = 1.5. The Reynolds number for both cases is fixed at Re = 55k. It is immediately evident that increasing CN has a significant effect on the cavitation cloud extend; in the high CN case, the vapour cloud extends up to 75% of the channel length and liquid fraction in its core is as low as 5%. Instead, in the low CN case a limited extend of cavitation structures is shown and liquid volume fraction as low as 55%. The observed differences in vapour production inside the flow channel were expected, since the pressure difference across the injection hole, as denoted by CN, is mainly responsible for the initiation and development of geometric cavitation. However, what was unexpected in these illustrations is a slight vortex-like vapour shape that appears around the axis of symmetry of the channel at the left-hand side of the cavitation cloud of CN = 2.1 case. It resembles a string-like shape with its tip facing the hole entrance. This is the vicinity where cavitation strings have been recorded by high-speed shadowgraphy experiments as it is verified in the bottom row standard deviation images, where variability is indeed increased at the hole entrance vicinity. Of course it is impossible for the time-averaged data of micro-CT to capture such a transient feature, however, the existence of the previously described shape may be closely related to increased vorticity in that location, which may be adequate to promote string formation. Finally, the same structures exist also in the lower CN case of 1.5; however, their intensity and lifetime is not as pronounced as at higher CN.

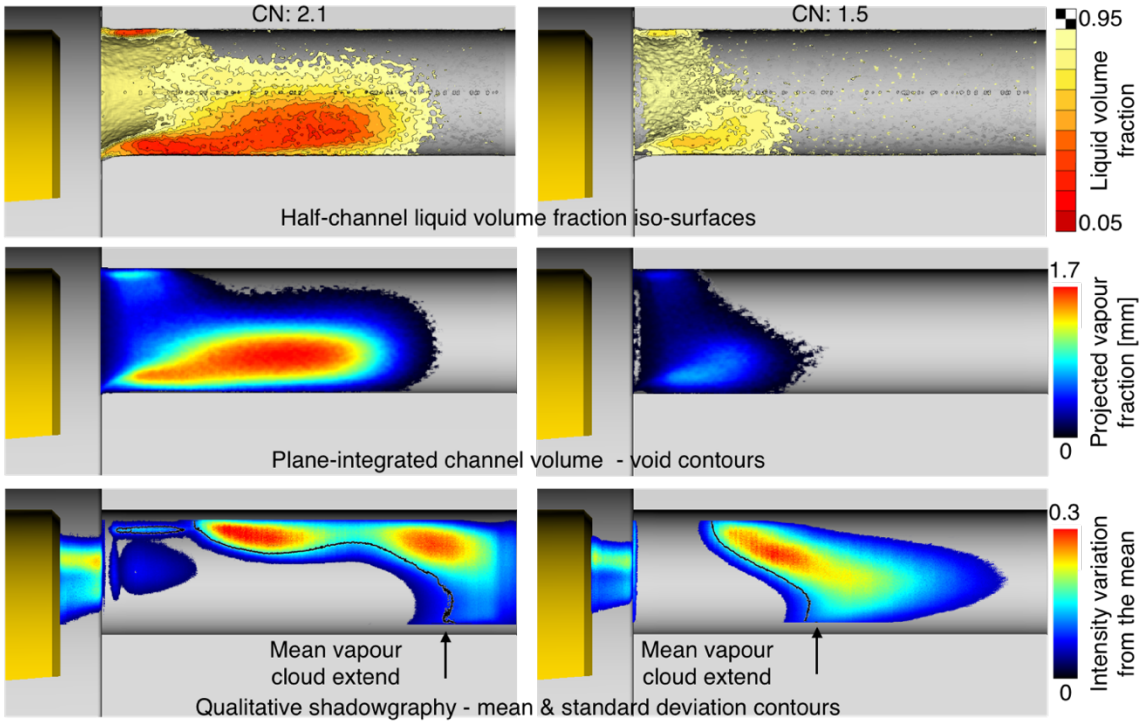

Figure 21: Effect of cavitation number (CN) on vapour pockets at fixed needle lift of 1mm and Reynolds number of 55k; (a) CN: 2.1 and (b) CN: 1.5.

Finally, Figure 22 illustrates the effect of Reynolds number on cavitation development. At a fixed CN = 1.5 and needle lift of 1mm, it is evident that an increase in Reynolds number from 35k (Figure 22a) to 55k (Figure 22b) has a marginal effect on vapour pockets inside the flow channel; increasing Re from 35k to 55k only resulted in marginally lower liquid volume fraction measured in the core of the vapour cloud and in marginally larger channel volume occupied by the highest void fractions (middle set of images in Figure 22), compared to Re = 35k. It should be noted that the false colour scale for the Reynolds number comparison ranges from 0.6 to 0.9, as opposed to the left-hand-side of Figure 21, where it ranges from 0.15 to 0.85; hence, the different contour colours for the case of CN = 1.5 and Re = 55k, which is identical in both columns of this figure. Finally, the transient behaviour of both cases is presented in the standard deviation shadowgraphy images (bottom row of Figure 22), where low Reynolds number showed increased variability in cavitation cloud shapes inside the channel, while the high Reynolds number demonstrated increased string cavitation activity at the entrance of the hole.

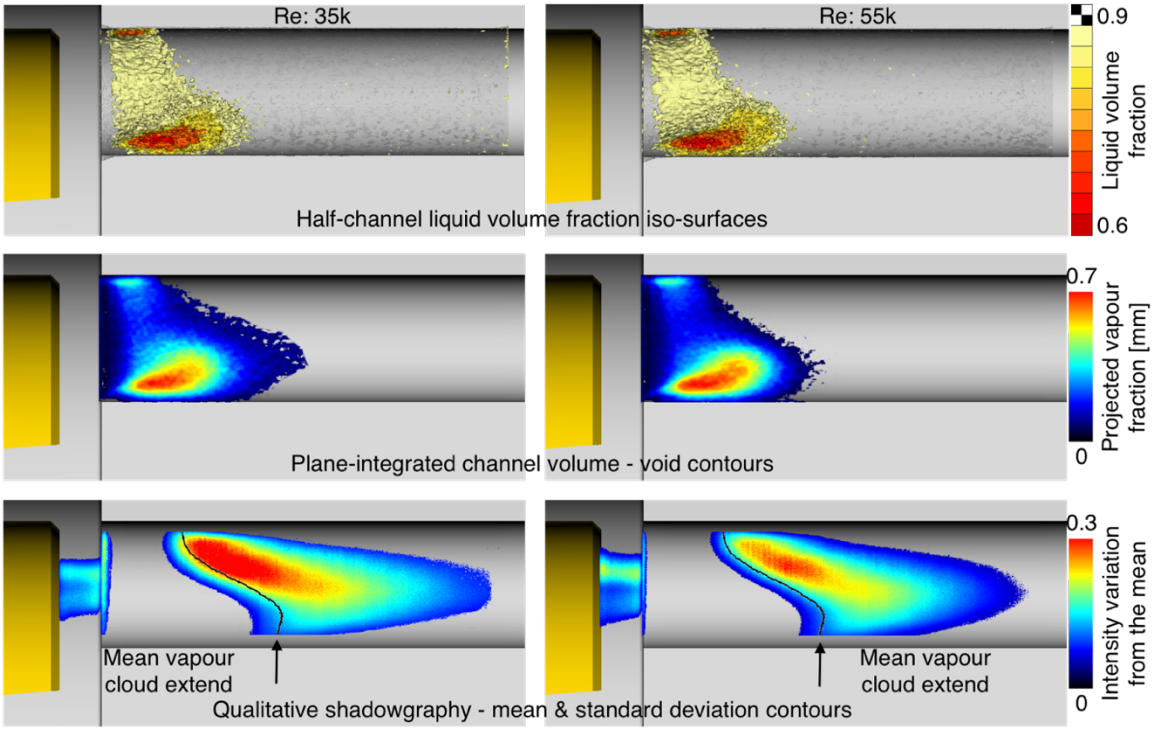

Figure 22: Effect of Reynolds number on vapour pockets at a fixed lift of 1mm and cavitation number of 1.5; (a) Re: 35k and (b) Re: 55k

Finally, the effect of dissolved gas in the fuel is illustrated in Figure 23. The fuel was degassed in a similar way to the flow visualisation degassing procedure described earlier. Results show no apparent difference between normal and de-gassed Diesel; however, a more detailed post-processing reveals: (i) vapour cloud extend for the de-gassed Diesel collapses marginally faster, while it occupies slightly larger volume of the flow channel, compared to normal Diesel, (ii) de-gassed Diesel showed sporadic liquid fraction values of the order of 0.1 inside the bulk vapour pocket, while normal Diesel showed lowest values of ~0.2 and (iii) vapour cloud structures of the de-gassed fuel demonstrated increased instabilities, compared to normal Diesel fuel. A hint of the latter behaviour has been given in [28], however, it has not been investigated fully. The two test cases of Figure 23 differ in Reynolds number, where the high CN case has a Reynolds number of 55k and the low CN case has a low Reynolds number of 35k. Illustrated images present liquid volume fraction iso-surfaces of 0.2 – 0.8 for CN = 2.1 and the respective values for the low CN case are 0.6 – 0.9. Moreover, normal Diesel is illustrated in the top row, while the second row of Figure 23 presents the corresponding images for the de-gassed Diesel case. Finally, the bottom row of the same figure depicts graphs of mean (diameter-wise) liquid volume fraction values versus normalised channel length. The discretisation for these graphs is provided by the lengthwise resolution of the micro-CT set-up, which was fixed at 15μm. Evidently, for the low CN case there is no measurable difference between the two fuels. On the other hand, the discussion in earlier paragraph, regarding the effect of condensed gas in the high cavitation number case, is verified by the mean liquid volume fraction values presented in the left-

hand-side graph. In detail, vapour starts building up at the sharp edge of the entrance of the channel similarly, for normal and de-gassed fuel; almost at 0.1 of the hole length, mean values differentiate and the de-gassed case shows lower liquid volume fraction, compared to the normal Diesel curve. Finally, after 0.6 of the hole length, where cavitation gradually collapses, the de-gassed Diesel case shows a more rapid collapse as opposed to the normal Diesel case.

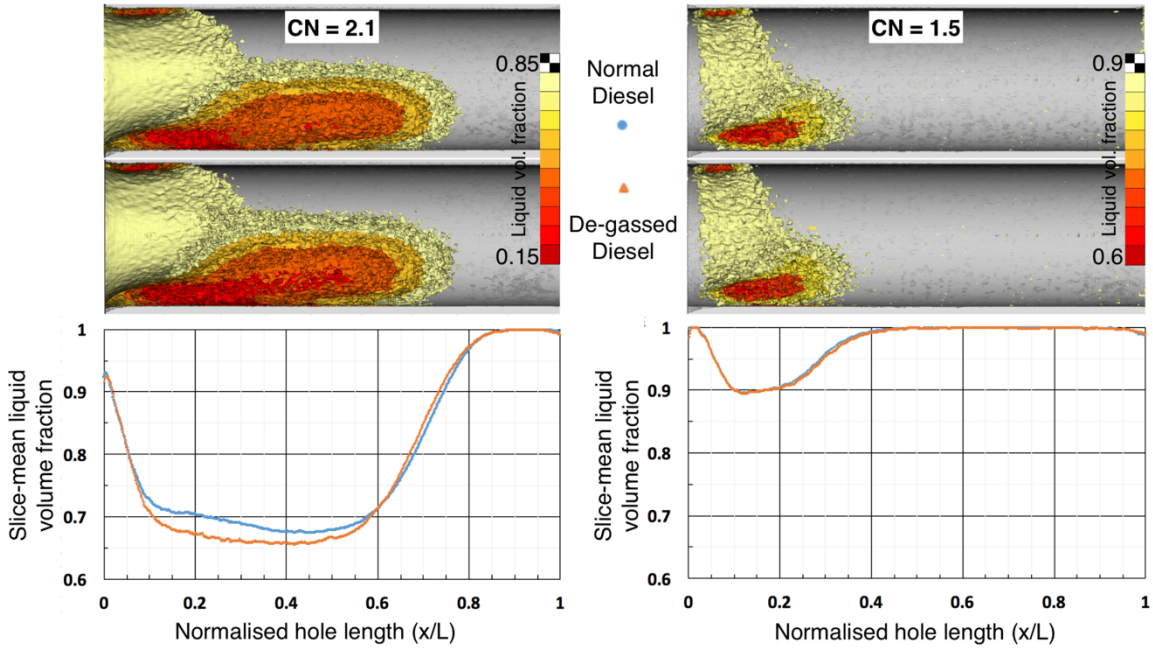

Figure 23: Comparison of mean distribution of liquid volume fraction along the hole length for normal and de-gassed Diesel at two operating points; CN = 2.1, Re = 55k and CN = 1.5, Re = 35k.

The last section of the WP4 results is dedicated to the effect of fuel properties and additives on cavitation structures. Table 3 presents all the fuels tested and their key properties. In detail, the Diesel surrogate is supplied by BP International Ltd. and it is a fuel made of only three components used to mimic normal Diesel mainly in CFD studies, where a simplified composition is advantageous. This surrogate fuel has slightly increased density compared to all others and larger viscosity compared to Base Diesel used. The second fuel in the table is the standard Diesel (Base Diesel for this study) without any additives. Base Diesel and all other additised fuels have been supplied by the Lubrizol Corporation. The fuels found in the two last columns of Table 3 are both additised fuels. The additive in both is intended to remove deposits that form inside a real Diesel injector during normal operation. The difference between the 'Traditional DCA' and the 'Power Gain' fuels is that the chemical composition of the additive is drastically different. In the first case, the traditional deposit control additive is used, while in the second case, a newly developed formula produced quaternary ammonium salts that actually act as a deposit removal additive. These salt molecules are electrically charged and this is one of the differences that stand out between the two additised fuels. The last fuel in the table (Power Gain – Fuel 2) is the one presented in the first periodic report and it was found to increase fuel flow rate with no apparent

change in operation, compared to the Base Diesel. Finally, it is important to note the differences in viscosity for all the fuels. Both additised fuels share a lower viscosity compared to Base Diesel.

Table 3: Tested fuels properties.

	DIESEL SURROGATE	**BASE DIESEL** – FUEL 1	**TRADITIONAL DCA**	**POWER GAIN** – FUEL 2
Composition	3 comp.	Multi-	Multi-/additised	Multi-/additised
Density @15°C	~882	860	850	850
Viscosity @40°C	<7	3.9	~1.5	~1.5

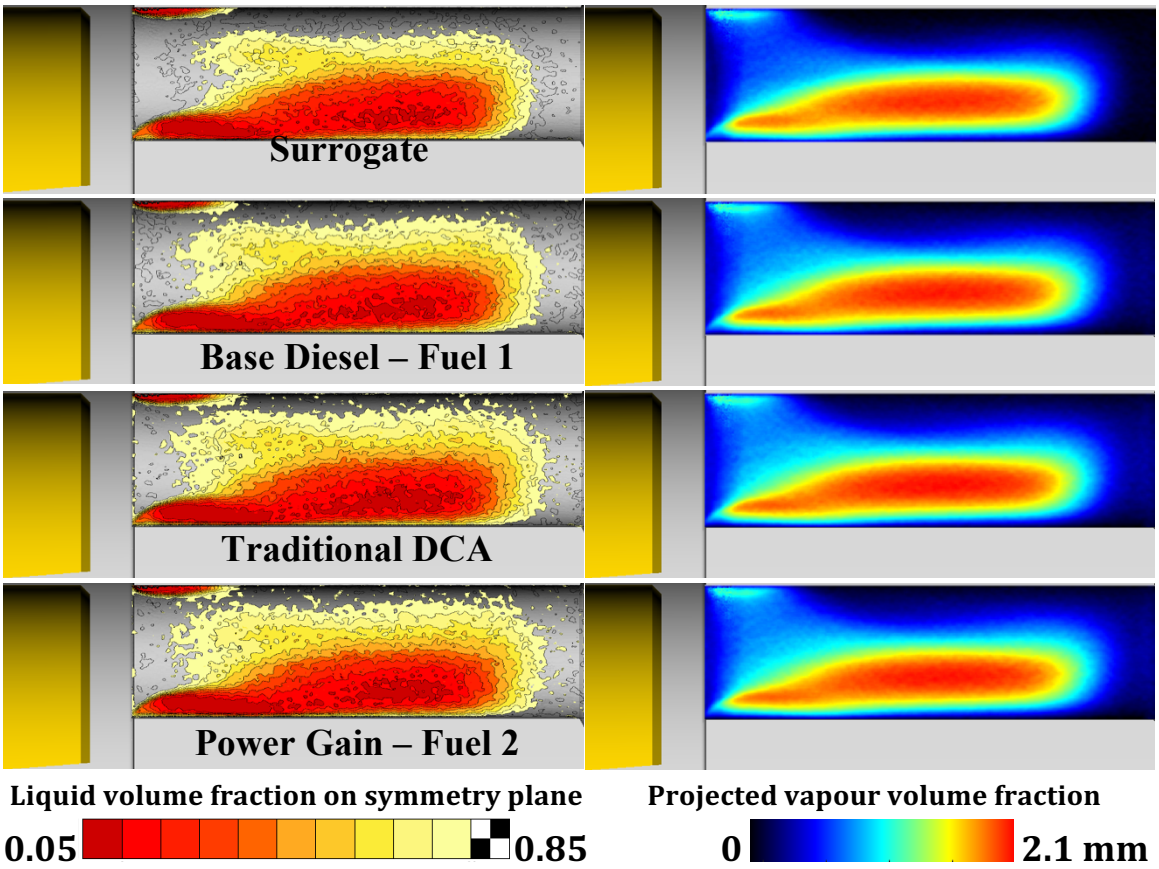

Figure 24: Comparison of all tested fuelsin terms of liquid volume fraction (left-hand-side) and projected vapour volume fraction (left-hand-side).

A direct comparison of X-ray micro-CT data as contour plots on the symmetry plane of the flow channel is illustrated in Figure 24, for a CN of 2.1, Re of 55k and needle lift of 1mm. Complementary images on the right-hand-side of Figure 24 illustrate the projected vapour volume fraction contours. The latter, as mentioned earlier, compresses all the information on vapour fraction across the diameter of the channel and presents it on a single plane. Nevertheless, one has to examine the results carefully in order to identify marginal

differences. All four fuels appear to have similar behaviour in terms of average liquid fraction inside the flow channel. In detail, the Diesel surrogate fuel reveals a slightly more confined vapour pocket, compared to the other three fuels. This is mainly attributed to its marginally higher density and higher viscosity. The other three fuels, the Base Diesel, the traditional and the new power gain additives look identical macroscopically. The only visible difference is a light spreading of the ~>0.7 liquid volume fraction occupied area in the case of the two additised fuels. However, this fact cannot justify the increase in fuel flow rate measured in WP3.

In an attempt to reveal any possibly hidden difference in these data sets, the fellow decided to produce some combination contour plots; thus, the Diesel surrogate data set was subtracted from the Base Diesel one. The reason for this action has been the confined cavitation pocket size of the surrogate fuel versus all other fuels. The results are illustrated in Figure 25. As expected, in the majority of the cross-sectional area of the symmetry plane the generated values are negative, which means that the surrogate fuel has higher liquid volume fraction values in this area than the Base Diesel. The latter was expected due to the contour plots of Figure 24. However, the unexpected behaviour was to observe positive liquid fraction values along the channel walls and only at the locations where cavitation exists. This outcome denotes the presence of Base Diesel next to the walls at larger fractions, as compared to the surrogate fuel. Effectively, this is interpreted as a thin layer next to the walls at the locations of cavitation of "more" liquid in the Base Diesel case rather than the surrogate fuel. One would expect the vapour cavity to be attached to the wall (fully detached flow), although, the latest results of this project confirm that this is probably a function of viscosity. The latter is the only difference between these two fuels (Table 3).

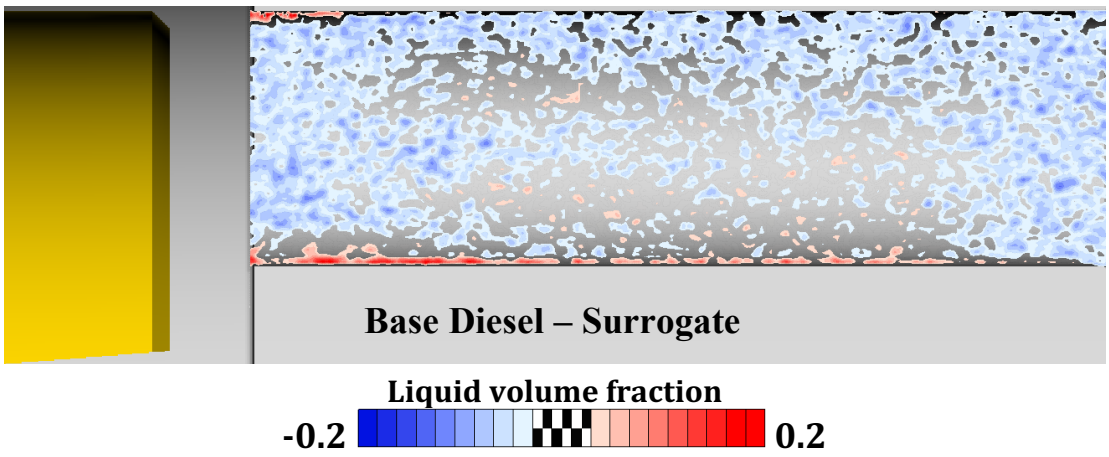

Figure 25: Subtraction of the Surrogate data set from the Base Diesel data set

The same post-processing was then applied to all other fuels, in order to obtain supporting evidence for the above preliminary conclusion. However, for the additive effect to stand out, the Base Diesel was treated as such and all other fuels were subtracted from it. Additionally, since the Power Gain (Fuel 2) additive was the only one showed increased fuel flow rates, we sourced the same additive in higher concentration in a similar batch of test-fuel. The

results are illustrated in Figure 26. The first contour plot shows that marginally there is higher liquid volume fraction of the Traditional DCA fuel next to the walls compared to the Base Diesel. This only happens on the bottom (as image is located) side of the flow channel, which is also the side with extensive vapour pockets; there is no evidence of positive liquid volume fraction values at the top side. It has to be noted here that this false colour-scale ranges from -0.1 to 0.1. On the contrary, both versions of the Power Gain fuel showed increased liquid volume fraction values next to the wall, compared to Base Diesel. Specifically, the higher the concentration of the additive (Power Gain High Concentration) the more pronounced the effect is. Additionally, the same additised fuel demonstrated some sporadic increased liquid volume fraction values in the bulk of the channel, compared to Base Diesel. Finally, it should be noted that the thickness of this layer is measured to be around 120μm.

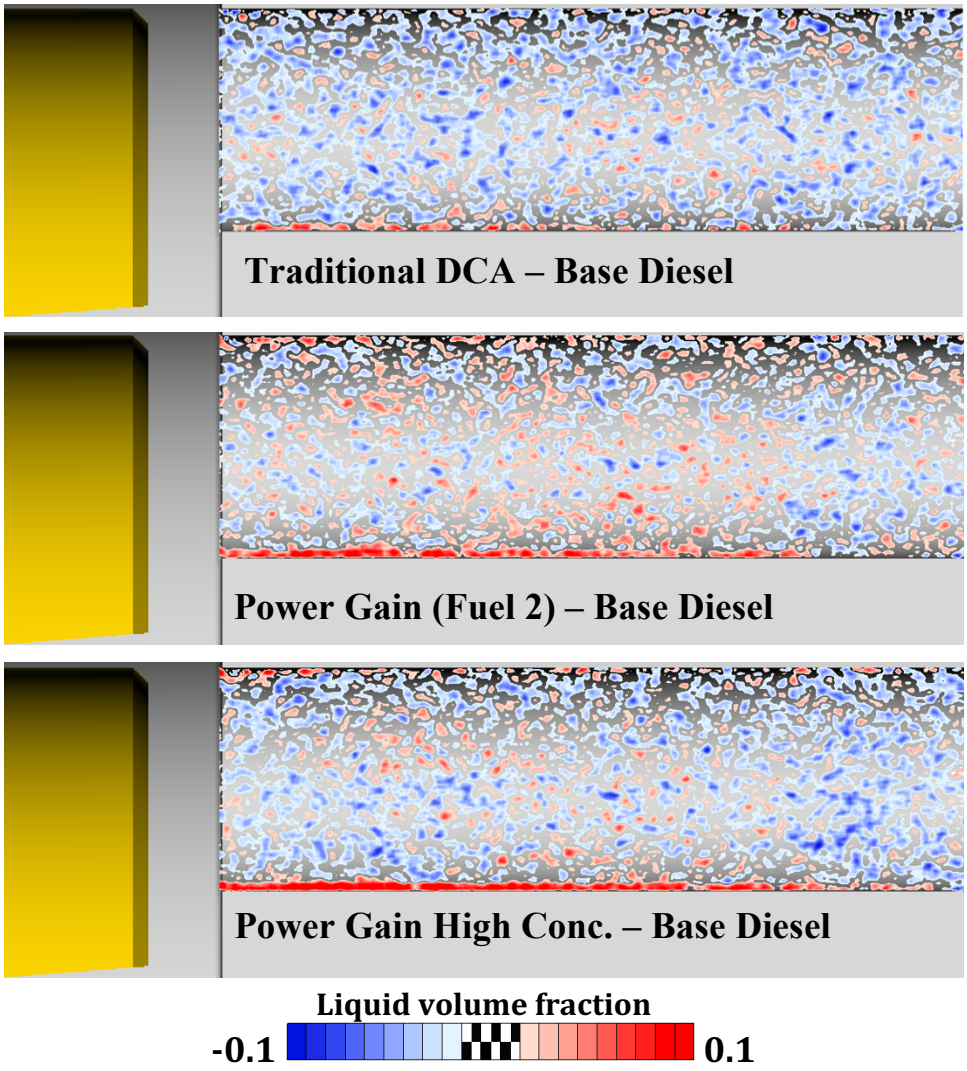

Figure 26: Contour plots of subtracted data sets of the Base Diesel from the additised fuels.

To summarise, the effect illustrated in Figure 25, between the Base Diesel and the surrogate fuel is possibly due to the differences in viscosity between the two fuels. On the contrary,

the effect shown in Figure 26 is not attributed to the viscosity difference solely. The reason is, even the Traditional DCA fuel shares the same viscosity value with the Power Gain fuel, their behaviour is not identical. Moreover, the Power Gain fuel demonstrates a more pronounced effect compared to the Traditional DCA fuel. The explanation behind this observation may lie in the chemistry of the latter additive; it has been discussed in earlier sections that this new additive molecule is a polymer-type molecule that has an electrically charged head group.

Following the major finding that links properties, chemistry and cavitation behaviour, X-rays micro-CT measurements revealed another known problem of Diesel nozzle injectors, this is erosion wear. As all measurements required calibration sets of an empty channel, these sets were then used to provide the internal channel geometry. The findings are impressive because of two reasons: (i) it is the first time that erosion wear has been recorded for a plastic test-nozzle at such low injection pressures (experiments used maximum injection pressure of 60bar) and (ii) the locations of erosion wear identified by extraction of geometry from the micro-tomographic data are in full agreement with the detached bubble clouds collapse locations recorded during visualisation studies and presented earlier in this section for the same WP4.

Figure 27 dictates that erosion develops in two distinct zones, at the nozzle wall exposed to cavitation: the first zone spans from ~1.4mm until 3.7mm downstream the nozzle entrance and the second zone from ~5.4mm until 8.8mm downstream the nozzle entrance. It must be highlighted here that this erosion development was recorded after testing under different cavitating conditions, so one cannot discern clearly the conditions that led to this erosion pattern. Undeniably though, at low cavitation number conditions, cavitation is mainly limited near the entrance of the hole, thus it is unlikely that the far downstream erosion site is caused by the low cavitation number operation.

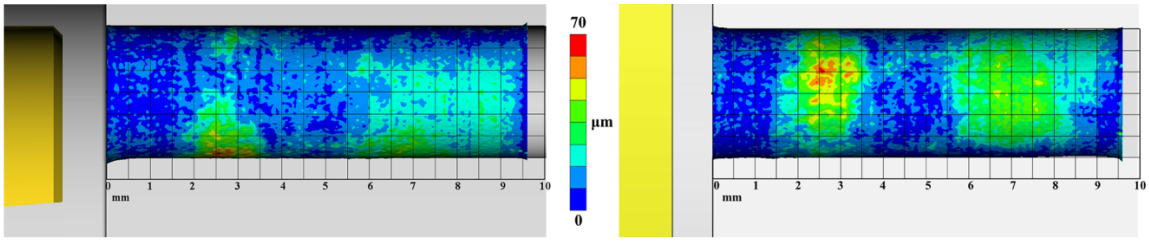

Figure 27: Erosion location as determined from CT scans of the geometry, expressed as the difference of the nozzle geometry prior and after exposure to cavitation for 40 hours.

WP5 – Objectives: CFD simulations of fuels of different properties and their effect on nozzle flow field.

D5: Interim progress report on computational investigations findings.

This work package is heavily dependent on the measured fuel properties from WP2 and the

results of the new WP4. We still were not able to measure the needed properties ourselves, however, our collaboration with Virginia Commonwealth University is on a good track and we expect to have results soon. Nevertheless, until these data become available, and given the experimental validation results produced from WP4, we collaborated with Lubrizol Corporation in identifying the prevailing mechanism that alters the flow once this specific type of additive is present. The outcome is fascinating and it is based on polymer behaviour, since the quaternary ammonium salt forms such complex structures.

As a continuation from the work presented in the first periodic report, in order to include the effect of polymers or surfactants in a Newtonian solvent, the extra viscoelastic stress tensor is computed from velocity gradients and added to momentum equations as a source term. In [29] they propose a model for the polymeric stress based on the network theory where the network junctions are created and destroyed by the elastic energy. Based on this model the constitutive equation for the stress tensor τ is:

$$f\big(tr(\tau)\big).\tau \; + \; \lambda\tau^{\nabla} = \; \mu_p(\nabla u + \; \nabla u^T) + \; \Gamma\,\nabla^2\tau$$

where:

$$f\big(tr(\tau)\big) = 1 + \; \varepsilon\frac{\lambda}{\mu_p}tr(\tau)$$

and τ^{∇} is the Oldroyd Upper Convected Derivative, defined as:

$$\tau^{\nabla} = \; \frac{D\tau}{Dt} - [\nabla u.\tau + \; \tau.\nabla u^T]$$

So rearranging the equation:

$$\lambda\,\frac{D\tau}{Dt} = \; \mu_p(\nabla u + \; \nabla u^T) + \lambda[\nabla u.\tau + \; \tau.\nabla u^T] - f\big(tr(\tau)\big).\tau + \; \Gamma\,\nabla^2\tau$$

And the elastic stress is added to the momentum equation:

$$\rho\frac{Du}{Dt} = \; -\nabla p + \; \mu_s\nabla.\nabla u + \nabla.\tau$$

In this equations, λ is the polymer relaxation time, μ_p and μ_s are the polymer viscosity and the solvent viscosity respectively and Γ is artificial diffusivity added for stability.

The model was validated in 2D and 3D in a channel flow and a sudden contraction geometry respectively. In order to define the additive properties, the following dimensionless numbers are used:

$$\beta = \frac{\mu_s}{\mu_0}$$

β is the ratio of the solvent viscosity to the total viscosity μ_0 (μ_s+μ_p), low values of β specifies a high molecular weight polymer or strong micelle network.

$$De = \frac{\lambda U}{D}$$

De is a measure of elasticity, it defines the ratio of the time scale of the fluid (λ is the polymer relaxation time) to the characteristic time scale of the flow. Higher De indicates the case where elastic effect prevails the viscous effect (high elasticity). The concentration of the polymer can be defined by the constant ε, which can be taken as 0.02 for dilute solutions.

The first validation case is a 2D channel flow where the effect of polymer viscosity on the normal and tangential elastic stress is studied. The CFD predictions are compared to the analytical solution of the viscoelastic channel flow [30].

(a) (b)

Figure 28: Computational grid (a) and the flow profile (b) for channel flow

Parabolic velocity profile is used for inlet boundary condition and a structured grid is used as shown in Figure 28. Comparison of the polymeric stress calculated by the code and the analytical solution is shown in Figure 29. The results show that by increasing the polymer viscosity (decreasing β), normal and tangential elastic stress are increasing. It is expected to have the highest stress values at regions of high velocity gradient, and it is evident from the graphs that the maximum stress values are near the wall and at the channel centreline where velocity gradient approaches zero, elastic stress also goes to zero. The values predicted by CFD match the analytically calculated values, giving confidence in code implementation.

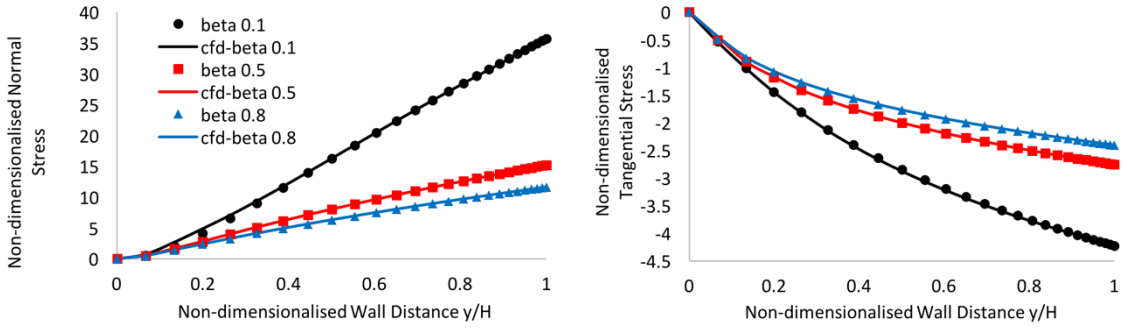

Figure 29: Effect of polymer viscosity on normal and tangential elastic stresses, comparison of CFD and the analytical solution for ε = 0.25 and De = 1.

Finally, the viscoelastic model is applied to a test case with cavitation to study the effects of viscoelasticity on cavitation formation and development. The selected test case is the one found in [31]. Two more test cases with the viscoelastic effect at high (β = 0.1) and low (β = 0.8) viscoelasticity are considered for the current study.

Fluids with viscoelastic properties are expected to have a lower turbulence level due to the stabilizing effect provided by the polymer or surfactant networks extension and relaxation. Consequently, the shear layer instabilities can be suppressed, reducing the vortex shedding frequency and hence increasing the length of the recirculation zone. The stabilizing effect and lengthening of the recirculation zone can be seen in Figure 30.

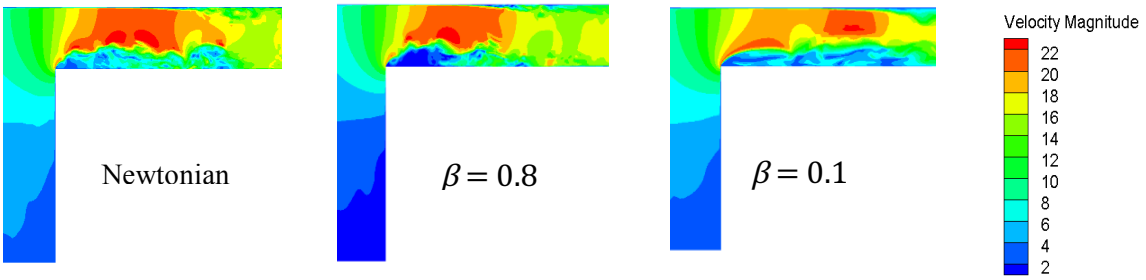

Figure 30:Indicative velocity magnitude contours for Newtonian and viscoelastic fluids

The isosurfaces and the contour of second invariant of the velocity gradient are shown in Figure 31 for the Newtonian and viscoelastic fluids to demonstrate the flow vortical structures. It can be seen that viscoelasticity causes the vortical structures to elongate and stabilize, as a result vortices in the shear layer are larger in the viscoelastic fluids and there are fewer microvortices and small scale eddies. Moreover, the spanwise vortices are inhibited in the viscoelastic fluids and in the case of β = 0.1 the dominant vorticity in the shear layer is in the streamwise direction. It is evident that the 3D structures are significantly suppressed especially in the case of β = 0.1 and the turbulence level at the nozzle exit is significantly reduced. Furthermore, fewer vortical structures are seen near the wall in the recirculation region of the viscoelastic fluids.

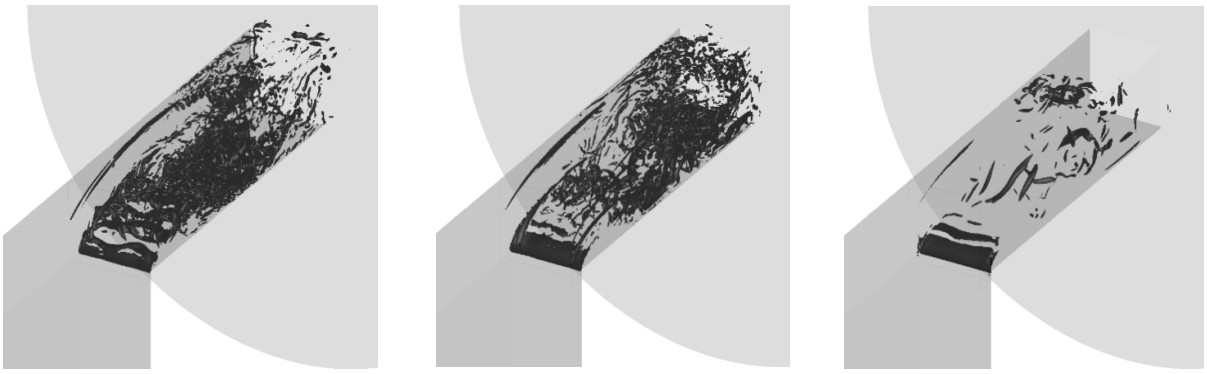

(a)

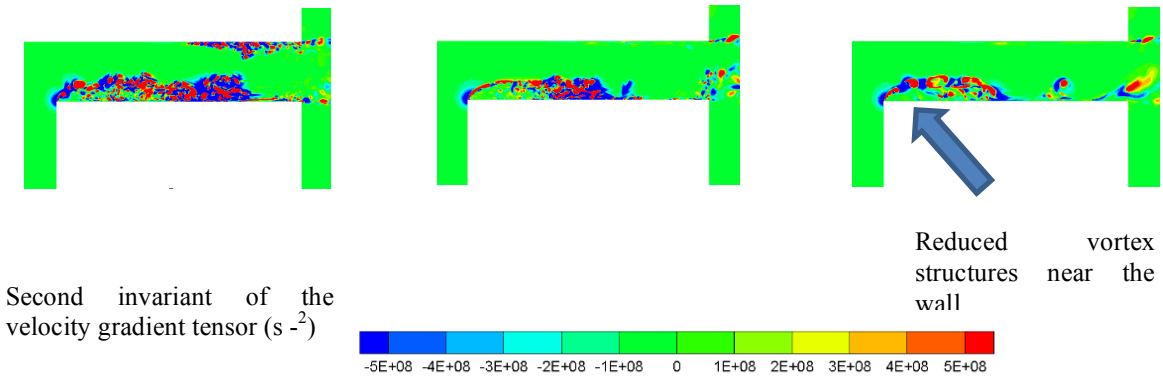

(b)

Figure 31: (a) Isosurface of second invariant of the velocity gradient at 2E+09 s-2 (b) and Contour of second invariant of velocity gradient in nozzle midplane.

Figure 32 shows the time averaged liquid volume fraction contours for the Newtonian and viscoelastic cases in the midplane of the nozzle. In case of β = 0.1 it can clearly be seen that the cavity volume is smaller than the Newtonian fluid and the cavity region is pushed away from the wall. This may be because the viscoelastic stress opposes the rotation of microvortices, hence preventing the formation of low pressure vortex cores. Also the eddies near the wall form some of the smallest cavitating microvortices and the viscoelastic stress may only be strong enough to oppose these microvortices and only elongate the larger cavitating vortices of the shear layer. Also in case of β = 0.8 the cavity length is slightly shorter compared to the Newtonian case.

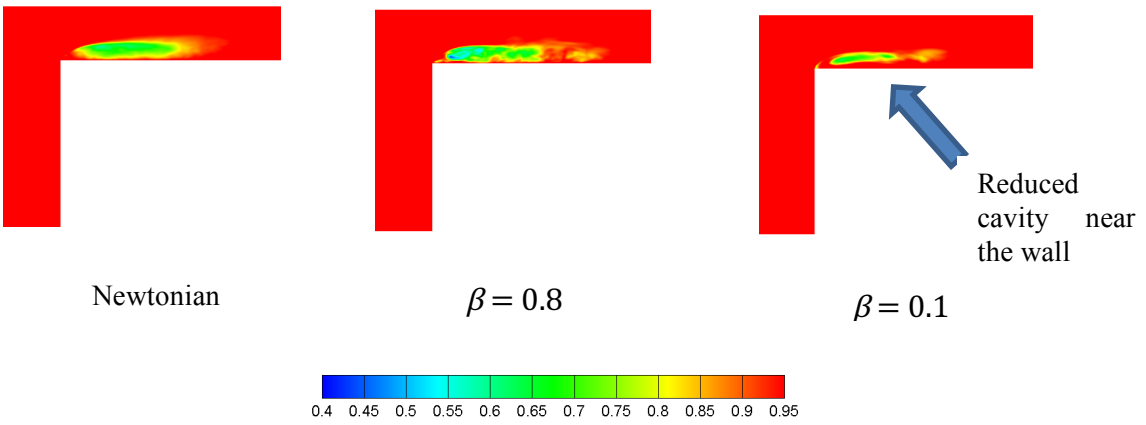

Figure 32: Time averaged liquid volume fraction for Newtonian and viscoelastic cases

Figure 33 shows the isosurafce of 70% iquid volume fraction for the three fluids. It is evident that the structure of the cavity is significantly altered by the viscoelastic effect in both cases. In the Newtonian case, appart from the large cavitating vortices, there are many smaller scale vortices shedding in the shear layer. Such small cavitating microvortices are far less visible in the case of case of β = 0.8 and they almost do not exist in the case of case of

β = 0.1. On the other hand, cavitating vortices in the shear layer are larger and have a more elongated shape compared to the Newtonian fluid. Moreover, in the highly viscoelastic case the cavity volume is mainly detatched from the nozzle wall. It is worth noting that even in the case of β = 0.8 where the fluid is not highly viscoelastic, the dynamics and structure of the cavitation has changed significantly.

Figure 33: Instantaneous Isosurface of 70% liquid volume fraction

WP6 – Objectives: Cavitation measurements and flow visualisation inside real-size transparent nozzles.

D6: Interim report of the effect of additives on cavitation behaviour inside real-size nozzles.

The main milestone and expected results of WP6 has been the full characterisation of cavitation inception and development inside real-size nozzles for different Diesel fuel blends. Following the tremendous progress achieved in this field in WP4 with the combination of high-speed visualisation and X-ray micro-CT measurements, it has been rendered impossible to observe the expected differences in a real-size nozzle. As presented earlier, cavitation development and initiation inside the large-scale flow channel has appeared to be almost identical for all tested fuel blends. Moreover, it has been demonstrated that the difference in the various blends lies only in a thin layer of liquid in-between a vapour cavity and the nozzle wall. This has been recorded in a large-scale model, where injection velocities do not exceed 60 m/s. On the contrary, in real-size nozzle holes the corresponding injection velocities inside one orifice do not fall below 300m/s and sometimes they may exceed 700m/s (depending on injection pressure). Given the available technological advances and equipment for high-speed techniques, it is a great challenge, if not impossible, to visualise a flow passage of 200μm with adequate resolution in order to capture the observed behaviour as in the large-scale model that is visible only as a thin interface layer between vapour cavities and the wall. Additionally, the results that revealed the breakthrough knowledge in the mechanism of these additives came from X-ray techniques. The tube X-ray source used in the course of this project is a laboratory scale

tube and lacks the characteristics that will enable quantitative high-speed radiographies to be collected. The latter is currently possible in synchrotron X-ray sources. Therefore, the fellow designed a new test section, featuring smaller dimensions than the current one and made of carbon fibre material. The rationale behind this decision is to produce a test nozzle whose diameter lies in the millimetre range (d=1.5mm) made from a material able of withstanding injection pressures up to 150bar. Such a test nozzle moves gradually towards the direction of smaller dimensions and higher injection pressures, targeting to mimic a real-size nozzle, at a step-by-step approach.

Nevertheless, the carbon fibre nozzle has been manufactures, and the test rig is currently shipped to the US, to the Argonne National Laboratory, where the next phase of experiments will be performed. This future phase includes high-speed quantitative radiographies that will reveal vapour volume fraction across the nozzle at an adequate resolution for a variety of operating conditions and fuel blends.

The new model design is illustrated in Figure 34; the hole diameter is now 1.5mm and its length is 5mm. The length is reduced, compared to the initial model, in order to maintain the same Length/Diameter ratio with the initial model for them to be comparable. The next differentiation is the shape of the hole entry; this is now changed to hemispherical shape (not flat) and the same design change applies for the needle valve, which is now hemispherical and not flat. The latter was dictated by the X-ray technique, as any surface parallel to the axis of X-rays will produce artefacts that may render the results not trustworthy. Additionally, the model has several thin layers of carbon fibre around the flow channel and its external shape resembles a “neck” around the injection hole. This is done to reduce the material thickness around the flow channel in order to limit X-ray attenuation.

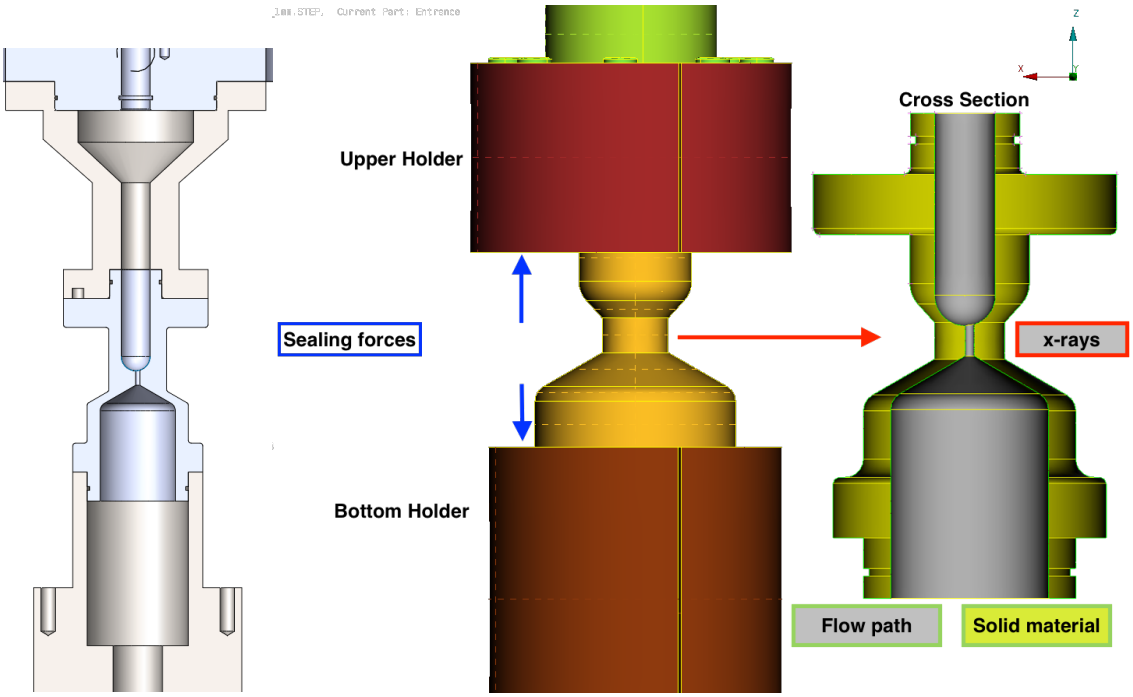

Figure 34: New model design.

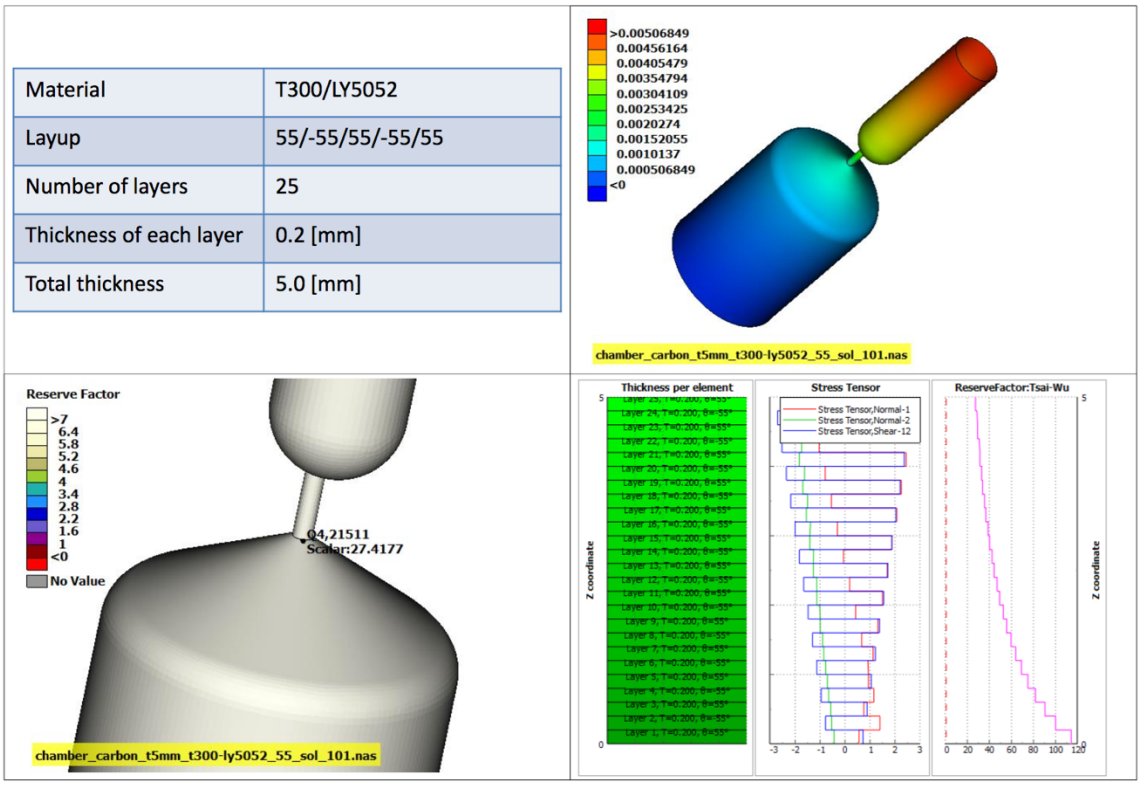

Figure 35: Finite element method analysis of the carbon fibre part to analyse its strength and maximum pressure limit.

A set of Finite Element Analyses (FEA) and several loading scenarios were simulated for the new model. It was treated as a laminate model (carbon fibre parts are simulated in this sense) and, as illustrated in Figure 35, simulations showed that a maximum injection pressure of 150bar can be achieved without problems at a part thickness of 5mm (at the neck) and 25 carbon fibre layers of 0.2mm each.

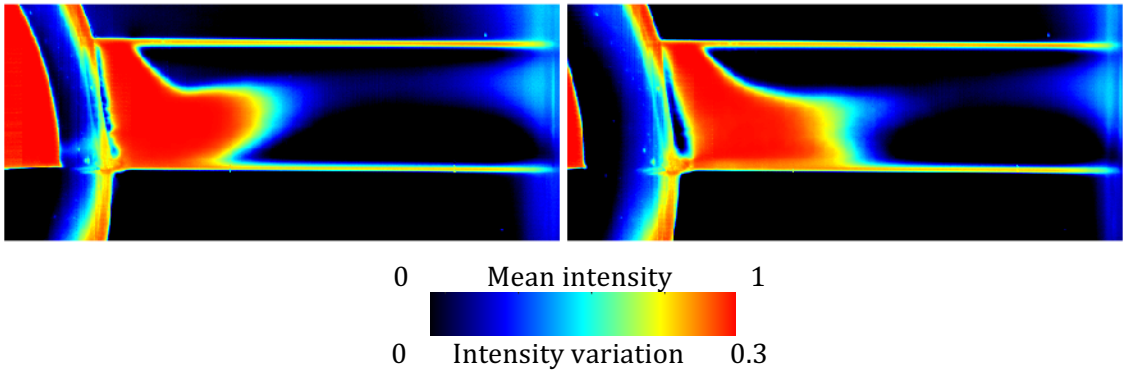

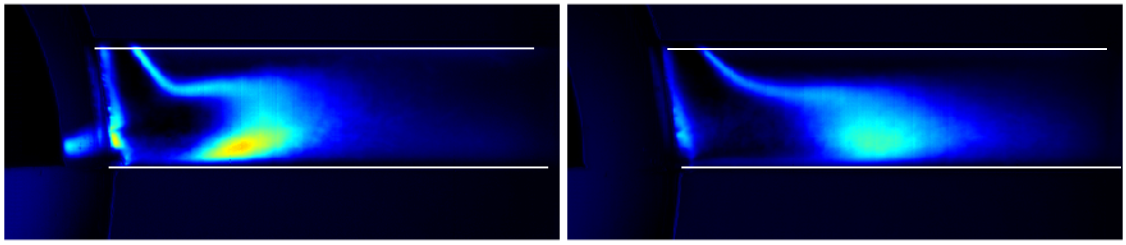

Figure 36: Preliminary visualisation results of new 1.5mm diameter model. Left-hand-side: needle lift of 0.5mm and righ-hand-side of 1mm. CN is 1.6 for both cases and Re is 15.5k

Some preliminary high-speed shadowgraphy results are illustrated in Figure 36. In detail, top row images are mean images and standard deviation images are seen in bottom row of Figure 36. Left-hand-side images refer to needle lift of 0.5mm, while at right-hand-side images the needle position is fixed at 1mm. The needle shape, as well as the sac volume hemispherical design can be clearly seen in the mean image of 0.5mm lift. Flow differences among the two test cases presented can be summarised as follows: (i) both cases present a similar extent of cavitation structures, however, the low needle lift case demonstrates a relative lift of the vapour cloud off the wall, compared to the needle lift case of 1mm, where vapour cloud seems to be attached to the wall. The above difference is also depicted in the standard deviation images, where an increased instability is visible towards the end of the bubble cloud and in contact to the channel wall. The same location in the needle lift of 1mm is features almost half the instability of the low needle lift case.

Finally, in the bottom row of Figure 36, increased variability can be identified in the low needle lift case. This is translated as a preference for string cavitation to appear in lower needle lifts. This has been seen also in the initial model of larger hole diameter; however, conclusions can be extracted only following a complete map of operating conditions for the 1.5mm diameter nozzle. Test cases of higher Reynolds number than 15.5k will probably give rise to more string cavitation to be visible at the vicinity of the channel entrance.

The presented cases only refer to Base Diesel fuel, as the experimental campaign is not finalised yet. Currently the test rig has been shipped to the USA and following successful completion of the high-speed densitometry experiments, a complete visualisation study including all fuels selected for this project will be carried out.

WP7 – Objectives: Dissemination of findings.

D7: Publication of journal and conference papers regarding the grant activities.

The activities of the current project have been disseminated with the following papers:

- Conferences
    - Presentation in the 2nd Cavitation Workshop, organised by the International Institute of Cavitation Research, Dec, 2013, London, UK
    - Presentation in the 3rd Cavitation Workshop, organised by the International Institute of Cavitation Research, Dec, 2014, London, UK

- Invited lecture in 13th International Conference on Future Engines for Vehicles, June 21-25, 2015, Port Jefferson, NY, USA
- Peer-reviewed paper in 9th International Symposium on Cavitation (CAV2015), December 6-10, 2015, EPFL, Lausanne, Switzerland [32]
- Presentation and 2 posters in the 4th Cavitation Workshop, organised by the International Institute of Cavitation Research, May 30 - June 1, 2016, Chania, Crete
- Peer-reviewed paper in 27th European Conference on Liquid Atomization and Spray Systems (ILASS), September 4-7, 2016, Brighton, UK.

- Journal publications
  - *Cloud cavitation vortex shedding inside an injector nozzle*. To be published in Proceedings of Royal Society A.
  - *Quantitative predictions of cavitation presence and erosion-prone locations in a high pressure cavitation test rig.* Under review in Journal of Fluid Mechanics.
  - *Application of X-ray micro computed tomography on high-speed cavitating Diesel fuel flows.* Under review in Experiments in Fluids.
  - *A novel technique for investigation of high-speed cavitating Diesel fuel flows by X-ray micro computed tomography.* Under review in Review of Scientific Instruments.
  - *Effect Diesel fuel additives on flow and its link to power gain effects.* To be submitted (journal has not been decided yet).

3 Conclusions

WP1 - Objectives: Literature review.

Task1.1: Identify Diesel fuel additives to be acquired for experimentation.

- Literature survey was successful, although not a large number of publications was identified for the topic. However, latest developments in the Diesel additives industry came across and in collaboration with one of our partners we identified the additives that are attractive in terms of fluid flow alteration.

Task1.2: Identify chemical composition of the selected types of additives.

- The fellow managed to identify the chemical family of the new additives in question, but not the exact chemical formulas. This was expected, as this industry is governed by proprietary compositions and patents.

WP2 - Objectives: Design/adaptation of suitable properties measurement techniques.

Task2.1: Literature review of available physical properties measurement techniques.

- Literature review on physical properties measurement techniques showed that development of such devices is not trivial. Knowledge acquired contributed to a careful scheduling for Diesel properties measurement and enhanced our quest for possible collaborations in the field.

Task2.2: Design of a test device for physical properties measurements.

- The design of a test device to measure the most important physical properties of additised Diesel fuel at exotic pressures in excess of 2000 bar proved extremely expensive and it could not be covered from the available funds for equipment. Therefore, the fellow requested help/collaboration from other laboratories that already have available equipment for this kind of measurements.

Task2.3: Measure physical properties of interest of additised Diesel fuels.

- The fellow managed to measure physical properties of interest at atmospheric pressure and at ambient temperature, however, properties variation at much higher pressures would be advantageous

WP3 - Objectives: Quantify the effects of additives on fuel injector performance.

Task3.1: Selection of injector type, based on fuel injector performance.

- Injector performance was measured in terms of fuel flow rate at various operating conditions for two widely used nozzle designs. Results proved inconclusive and a strategic decision was taken to focus on the fundamental study of the effect of additives on cavitation. The latter was proved difficult on multi-hole nozzle designs, as the hole-to-hole interactions and the highly transient operation of the needle valve during an injection event introduced phenomena that limited our ability to isolate and study cavitation initiation and development. Thus, we designed a new prototype single hole large-scale nozzle that we believe serves the purpose quite well, as preliminary results showed.

Task3.2: Instrumentation set-up.

- Following the design and manufacture of the prototype nozzle to be used, appropriate instrumentation was installed in key positions in order to provide valuable localised measurements of pressure and flow rate during experiments

WP4 - Objectives: ~~Experimental investigation on Diesel injector sprays formation and atomisation characteristics and how it is affected by the properties of selected additives.~~ Qualitative and quantitative investigation on cavitation formation and development characteristics for various Base and additised Diesel fuels using high-speed visualisation

(qualitative) and high spatial resolution computed tomography (quantitative) techniques, and how this is affected by the properties of selected additives.

Task4.1: Digital high-speed imaging.

- High-speed visualisation has provided useful insight on the transient features of cavitating fuel flows, such as string cavitation, bubble cloud vortex shedding and vapour pocket topology variability. All results are qualitative, but they do capture the transient nature of the phenomena. Processing of the high-speed images has revealed similarities between nozzle flow and flow around a hydrofoil, in terms of vortex shedding and the associated mechanism. Additionally, recording of collapse locations of previously detached bubble vortices indicated erosion-prone locations, that were later validated by the computed tomography data by extraction of the channel exact geometry. Finally, the effect of fuel additives and dissolved gas in the fuel on the transient feature of vortex shedding is still under investigation and data sets are currently being post-processed.

Task4.2: ~~Phase-Doppler anemometry~~. Micro Computed Tomography (CT).

- The strategic decision of including X-ray micro-CT experiments in this grant has proven to be of great value. Results obtained from quantitative micro-computed tomography revealed a variety of features and mechanisms, not only on the effect of additives on fuel flows, but also on the effect of several flow parameters on cavitation structures. Effects of needle lift, CN and Re on cavitation had been studied extensively; however, the lack of quantitative data was a major drawback for the development of newer and better CFD models than the existing ones. This gap has now been bridged and requests for sharing the micro-CT results with the CFD community are of great importance. Additionally, the use of X-ray techniques has assisted in the understanding of the mechanism that certain chemical types of fuel additives affect fuel flow and interact with vapour cavities. Despite the limitations of a laboratory scale X-ray source that dictated the production of averaged quantitative data, coupling of the averaged data with high-speed shadowgraphy results proved to be advantageous, as the mean liquid volume fraction values measured are better connected to the transient nature of the flow, enhancing our understanding. Finally, extraction of the channel geometry after several hours of operation has revealed erosion wear at locations that coincide very well to the erosion-prone locations extracted from high-speed imaging. It is worth noting that nozzle material removal depth had been measured to be as deep as 70μm, locally.

WP5 - Objectives: CFD simulations of fuels of different properties and their effect on nozzle flow field.

Experimental results from WP4 have greatly contributed towards the enhancement of understanding and development of CFD model to capture the behaviour of polymers and

surfactants present in fuel solutions. The model has demonstrated its ability to capture differences in cavitation development in simple validation cases. Currently, the simulation of the complete test nozzle is under way and results are expected to be in good agreement to the quantitative measurements of liquid volume fraction obtained in WP4.

WP6 - Objectives: Cavitation measurements and flow visualisation inside real-size transparent nozzles.

As described in previous section, it has been decided to decrease the dimensions of the current nozzle to half, and double the injection pressure, rather than using a real-size injector that scales down 10 times in dimensions and scales up 30 times in injection pressure. The new model has already been manufactured and has been shipped to the Argonne National Labs of USA for further experimentation using high-speed synchrotron sources. Nevertheless, preliminary high-speed visualisation experiments demonstrated that the new design has successfully fulfilled its purpose and the flow field inside the injection hole is now closer to a real Diesel nozzle. The reduction of its diameter to half (5mm) has given rise to a variety of phenomena to be visualised mainly due to the increased range of operating conditions; Reynolds numbers and cavitation numbers span now across larger ranges, as opposed to the initial model. Finally, post-processing of the densitometry results obtained at a synchrotron source will clarify if the recorded behaviour of additised fuels at the large scale model is also captured at the smaller dimensions test-rig.

WP7 - Objectives: Dissemination of findings.

During the course of this project the fellow has managed to inform students in several institutions about the FP7 Marie Curie actions and their targets. The best opportunities for such informative talks have been Open Days at the outgoing and returning host institutions, as well as at similar occasions at several other establishments, such as EPFL, MIT, Bergamo University, University of Brighton, Technological Institute of Pireus and Mediterranean Agronomic Institute of Chania.

The activities of this grant and the associated results have been presented at 6 international conferences; some of the most prestigious international conferences in cavitation are included, such as CAV. Also, the activities have been presented at a well established conference of all major worldwide engine manufacturers, where the fellow and the scientist in charge had been invited to present the latest findings in cavitation in Diesel nozzles and the effects of fuel properties and additives on fuel flow. A similar workshop of PhD students hosted by Lubrizol Corporation has been another occasion, where a number of researchers attended poster sessions and talks related to this activity. Additionally, the work done under this grant has attracted interest from BP International Ltd, Caterpillar and Delphi Diesel Systems.

Finally, the work done in the course of this fellowship has produced 5 journal publications. All manuscripts are currently either under review or have just been sent to the editor; the reason of them not being public yet is the fact that the majority of important findings and

conclusions happened during the last year of this fellowship. Thus, manuscripts are still being edited and enriched with newly processed data.

The work undertaken now at the ANL facilities in the USA are expected to produce another 1-2 journal publications and a similar number of conference papers.

4 References

1. Technical Committee of Petroleum Additive Manufacturers in, E., *Fuel Additives: Use and Benefits*. 2013.
2. Owen, K., *Gasoline and diesel fuel additives*. 1989: New York, NY; John Wiley and Sons Inc.
3. Owen, K. and T. Coley, *Automotive fuels reference book*. 1995.
4. Barbour, R., et al. *Fuel Additive Induced Power Gain Phenomenom in Diesel Engines*. in *Fuels 2015, 10th International Colloquium*. 2015.
5. Barbour, R., R. Quigley, and A. Panesar, *Investigations into Fuel Additive Induced Power Gain in the CEC F-98-08 DW10B Injector Fouling Engine Test.* SAE Technical Paper 2014-01-2721, 2014. **SAE Technical Paper 2014-01-2721**.
6. Barbour, R.H., *Method to Provide Power Gain in an Engine*. 2011.
7. Roder, H.M., *A transient hot wire thermal conductivity apparatus for fluids.* Journal of Reseach of the Natioinal Bureau of Standards, 1981. **86**(5): p. 457-493.
8. Caudwell, D.R., et al., *Viscosity and Density of Five Hydrocarbon Liquids at Pressures up to 200 MPa and Temperatures up to 473 K†.* Journal of Chemical and Engineering Data, 2008. **54**(2): p. 359-366.
9. Caudwell, D.R., et al., *The Viscosity and Density of n-Dodecane and n-Octadecane at Pressures up to 200 MPa and Temperatures up to 473 K.* International Journal of Thermophysics, 2004. **25**(5): p. 1339-1352.
10. Harris, K.R., R. Malhotra, and L.A. Woolf, *Temperature and Density Dependence of the Viscosity of Octane and Toluene.* Journal of Chemical and Engineering Data, 1997. **42**(6): p. 1254-1260.
11. Malhotra, R., W.E. Price, and L.A. Woolf, *Thermodynamic properties of pentan-3-one at temperatures from 278 K to 338 K and pressures from 0.1 MPa to 380 MPa.* The Journal of Chemical Thermodynamics, 1993. **25**(3): p. 361-366.
12. Baled, H., et al., *Exploratory characterization of a perfluoropolyether oil as a possible viscosity standard at deepwater production conditions of 533 K and 241 MPa.* International Journal of Thermophysics, 2013. **34**: p. 1845-1864.
13. Baled, H.O., et al., *Viscosity of n-hexadecane, n-octadecane and n-eicosane at pressures up to 243 MPa and temperatures up to 534 K.* Journal of Chemical Thermodynamics, 2013. **72**: p. 108-116.
14. Zolghadr, A., M. Escrochi, and S. Ayatollahi, *Temperature and composition effect on CO2 miscibility by interfacial tension measurement.* Journal of Chemical and Engineering Data, 2013. **58**: p. 1168-1175; 1168.
15. Gustafsson, S.E., *Transient plane source techniques for thermal conductivity and thermal diffusivity measurements of solid materials.* Review of Scientific Instruments, 1991. **62**(3): p. 797-804; 797.
16. Warzoha, R.J. and A.S. Fleischer, *Determining the thermal conductivity of liquids using the transient hot disk method. Part II: Establishing an accurate and repeatable experimental methodology.* International Journal of Heat and Mass Transfer, 2014. **71**: p. 790-807.
17. Gavaises, M., et al., *Characterization of string cavitation in large-scale Diesel nozzles with tapered holes.* Physics of Fluids, 2009. **21**: p. 052107.
18. Gavaises, M., *Flow in valve covered orifice nozzles with cylindrical and tapered holes and link to cavitation erosion and engine exhaust emissions.* Int. J. of Engine Research, 2008. **9**(6): p. 435-447.
19. Gavaises, M., et al. *Comparison of cavitation formation and development in Diesel VCO nozzles with cylindrical and converging tapered holes*. in *THIESEL 2008*.

20 Ganesh H., Mäkiharju S. A., and Ceccio S. L., 2015, "Interaction of a Compressible Bubbly Flow With an Obstacle Placed Within a Shedding Partial Cavity", Journal of Physics: Conference Series, **656**(1), p. . 012151.

21 Mäkiharju S. A., Gabillet C., Paik B. -G., Chang N. A., Perlin M., and Ceccio S. L., 2013, "Time-resolved two-dimensional X-ray densitometry of a two-phase flow downstream of a ventilated cavity", Experiments in fluids, **54**(7), p. . 1-21.

22 Sun T., Ganesh H., and Ceccio S., 2015, "X-ray densitometry based void fraction flow field measurements of cavitating flow in the wake of a circular cylinder", Bulletin of the American Physical Society, **60.**

23 Mitroglou N., Lorenzi M., Santini M., and Gavaises M., 2016, "X-ray micro-computed tomography for cavitating Diesel nozzles", 27th Annual Conference on Liquid Atomization and Spray Systems.

24 Gavaises M., Villa F., Koukouvinis P., Marengo M., and Franc J. -P., 2015, "Visualisation and les simulation of cavitation cloud formation and collapse in an axisymmetric geometry", International Journal of Multiphase Flow, **68**, p. . 14-26.

25 Kolev N. I., 2007, "Thermodynamic and transport properties of diesel fuel", Multiphase Flow Dynamics 3, p. . 269-302.

26 Santini M., Guilizzoni M., and Fest-Santini S., 2013, "X-ray computed microtomography for drop shape analysis and contact angle measurement", J Colloid Interface Sci, **409**, p. . 204-10.

27 Duke D. J., Kastengren A. L., Swantek A. B., Sovis N., Fezzaa K., Neroorkar K., Moulai M., Powell C. F., and Schmidt D. P., 2014, "Comparing Simulations and X-ray Measurements of a Cavitating Nozzle", Proc of the ILASS-Americas 26th Annual Conference on Liquid Atomization and Spray Systems.

28 Duke D., Swantek A., Kastengren A., Fezzaa K., and Powell C., 2015, "Recent developments in X-ray diagnostics for cavitation", SAE Int. J. Fuels Lubr, **8**(1), p. . 135-146.

29 Thien N. P., and Tanner R. I., 1977, "A new constitutive equation derived from network theory", Journal of Non-Newtonian Fluid Mechanics, **2**(4), p. . 353-365.

30 Cruz D. O. A., de Pinho F. T., and Oliveira P. J., 2005, "Analytical solutions for fully developed laminar flow of some viscoelastic liquids with a Newtonian solvent contribution", Journal of non-newtonian fluid mechanics, **132**(1), p. . 28-35.

31 Sou A., Biçer B., and Tomiyama A., 2014, "Numerical simulation of incipient cavitation flow in a nozzle of fuel injector", Computers & Fluids, **103**, p. . 42-48.

32 Mitroglou N., Lorenzi M., Santini M., Gavaises M., and Assanis D., 2015, "Application of cone-beam micro-CT on high-speed Diesel flows and quantitative cavitation measurements", Journal of Physics: Conference Series, **656**(1).